REPORT DOCUMENTATION PAGE

Form Approved
OMB No. 0704-0188

Public reporting burden for this collection of information is estimated to average 1 hour per response, including the time for reviewing instructions, searching data sources, gathering and maintaining the data needed, and completing and reviewing the collection of information. Send comments regarding this burden estimates or any other aspect of this collection of information, including suggestions for reducing this burden to Washington Headquarters Services, Directorate for Information Operations and Reports, 1215 Jefferson Davis Highway, Suite 1204, Arlington, VA 22202-4302, and to the Office of Management and Budget, Paperwork reduction Project (0704-0188), Washington DC 20503.
PLEASE DO NOT RETURN YOUR FORM TO THE ABOVE ADDRESS.

1. REPORT DATE (DD-MM-YY) 11-29-99	2. REPORT TYPE FINAL	3. DATES COVERED (From – To) FROM:01-07-97 TO:31-03-99

4. TITLE AND SUBTITLE	5a. CONTRACT NUMBER

Physiological Vibration and Resonance of LFS on the Respiratory System

5b. GRANT NUMBER
N0014-97-1-0928

5c. PROGRAM ELEMENT NUMBER

6. AUTHOR(S)

Andrew C. Jackson, Ph. D.

5d. PROJECT NUMBER
98PR03048-00

5e. TASK NUMBER

5f. WORK UNIT NUMBER

7. PERFORMING ORGANIZATION NAME(S) AND ADDRESS(ES)
Trustees of Boston University
881 Commonwealth Ave.
Boston, MA 02215

8. PERFORMING ORGANIZATION REPORT NUMBER

9. SPONSORING/MONITORING AGENCY NAME(S) AND ADDRESS(ES)
Office of Naval Research
Ballston Centre Tower One
800 North Quincy St.
Arlington, VA 22217-5660

10. SPONSOR/MONITOR'S ACRONYM(S)
ONR

11. SPONSORING/MONITORING AGENCY REPORT NUMBER

12. DISTRIBUTION AVAILABILITY STATEMENT

APPROVED FOR PUBLIC RELEASE

13. SUPPLEMENTARY NOTES

14. ABSTRACT   Model predictions of the effects of LFS on the human respiratory system suggested that pressures within airways can be greater than pressures applied to the body surface. In the current study, more physiologically and anatomically accurate human and rat lung models were developed to further study the consequences of LFS as well as to infer human lung behavior from measurements made in rats. The human model was also used to predict whether pressure amplification would be more significant in asthmatics by incorporating airway heterogeneity and broncho-constriction into the model. Pressure amplification was predicted to be reduced in asthmatics. A comparison between human and rat lung behavior indicated that resonances in rat lungs occur in human lungs at about one-tenth the frequency. Thus, the resonances predicted to occur in rat lungs at higher frequencies, i.e., 5,000 and 11,000 Hz, could produce pressure amplification in humans at much lower frequencies (i.e., 50-100 Hz). We are confident in the human model predictions since they compared very well with physiological measurements over a wide frequency range (2-2000 Hz). However, we have less confidence in the rat model since it could be validated only for a limited frequency range (20-80 Hz) due to the paucity of published rat data.

15. SUBJECT TERMS
Lung barotrauma, respiratory system mechanical impedance, airway pressures, computer predictions of lung behavior

16. SECURITY CLASSIFICATION OF:			17. LIMITATION OF ABSTRACT	18.NUMBER OF PAGES	19a. NAME OF RESPONSIBLE PERSON
a. REPORT U	b. ABSTRACT U	c. THIS PAGE U	SAR		Andrew C. Jackson, Ph. D.

19b. TELEPHONE NUMBER (Include area code)
(617) 353-2833

Standard Form 298 (Rev. 8-98)
Prescribed by ANSI Std Z39-18

FINAL REPORT: PHYSIOLOGICAL VIBRATION AND RESONANCE EFFECTS OF LOW FREQUENCY SOUND ON THE RESPIRATORY SYSTEM

GRANT NUMBER: N00014-97-1-0928

PROJECT NUMBER: 98PR03048-00

SUBMITTED BY: Andrew C. Jackson, Ph.D.

INSTITUTION: Biomedical Engineering Department
Boston University
Boston, MA 02215

SUBMISSION DATE: February 2, 2000

Table of Contents

List of Figures

List of Tables

1. Introduction

The prime function of the respiratory system is to exchange oxygen from the air into the venous blood and carbon dioxide from venous blood to air. Gases are transported between the environment to the alveoli by convection. The pulmonary airways bifurcate in a treelike structure as shown in Fig. 1 [16]. Hence the geometry of the airways, such as diameters and lengths, airway wall thickness, and branching patterns are essential physical properties of the system that significantly influence the transport of respiratory gases.

. STRUCTURE AND FUNCTION
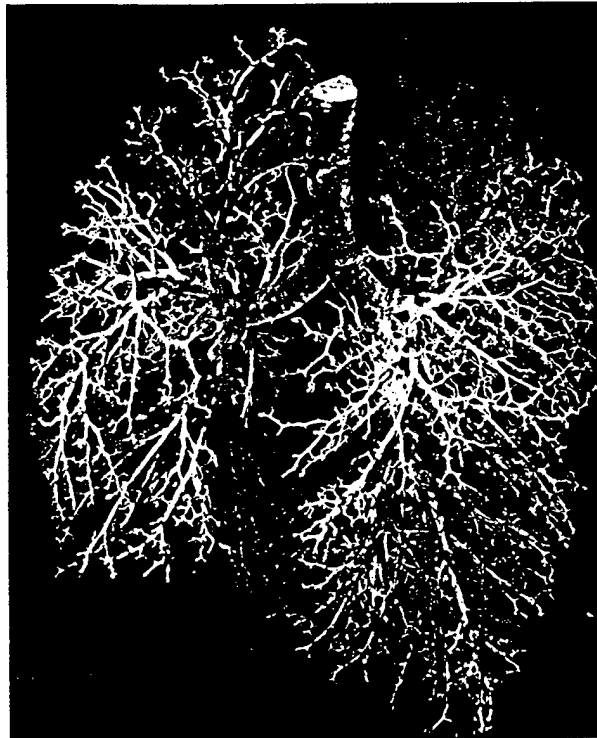
Figure 1. Cast of the airways of a human lung. The alveoli have been pruned away, but the conducting airways from the trachea to the terminal bronchioles can be seen [16].

The forced oscillation technique is a widely used approach to extract insight into how the structure of the lung (airway geometry and mechanical properties) influences it's function. There are two common methods for applying forced oscillations to measure mechanical impedance. One is to impose forced oscillations at the airway opening and measure the complex ratio of airway opening pressure P_{ao} to flow $\dot{V}_{ao}$, which yields input impedance $Z_{in}=P_{ao}/\dot{V}_{ao}$ [6, 25]. The other is to apply forced oscillations around the chest wall P_{cw} and measure transfer impedance defined as $Z_{tr}=P_{cw}/\dot{V}_{ao}$ (Fig. 2). In either case, the impedance spectrum is analyzed to understand the mechanical properties of the respiratory system. Conceptually, the respiratory system is comprised of airways and tissues separated by a volume of compressible alveolar gas. The mechanical properties and morphometric structure of the airways and tissues produce effective resistances, inertances and compliances, which all effect the overall impedance spectrum.

(α) Transfer Impedance System
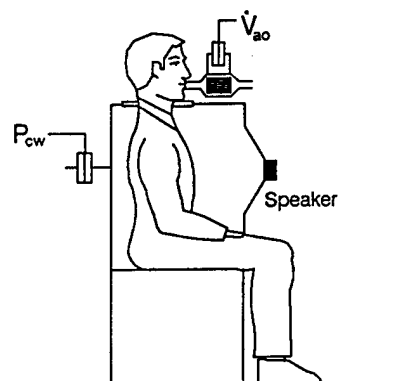
(b) Input Impedance Systems

Standard Method: Z_{st}
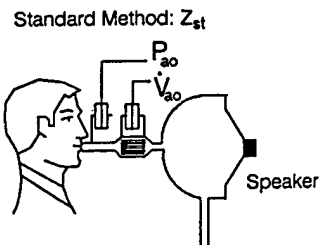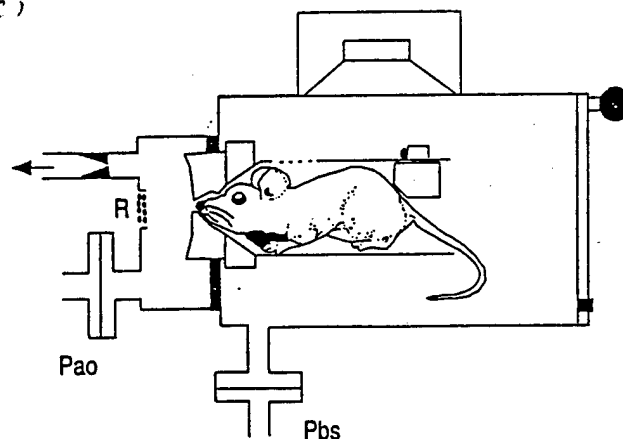
— Experimental set-up. The conscious mouse, placed in the modified Battelle tube in the body box, respires from the front chamber. To prevent rebreathing, the front chamber is flushed with a bias flow. R: wiremesh screen resistance; Pbs: pressure in the body box (body surface); Pao: pressure in the front chamber (airway opening).

Figure 2. (a) and (b) Schematic of measurement systems for input and transfer impedances in humans, respectively [6]. (c) Schematic of measurement system for transfer impedance in rats [25].

A theoretical study of a dog lung model predicted that with forced oscillations imposed at the airway opening, the alveolar pressure P_{alv} could be higher than the applied pressure P_{ao} at low frequencies (below 8 Hz) [20]. The question remained whether similar pressure amplification would occur in the human lung. Furthermore, would there be pressure amplification within the airways when the oscillations are applied to the body surface? Should there be any pressure amplification, what would be the implication for patients with bronchoconstriction?

The main goals of this study were to investigate the lung mechanics, including input impedance (Z_{in}), transfer impedance (Z_{tr}), as well as pressure, strain, and wave propagation distributions, in order to answer these questions.

The computational predictions were based on the symmetrical and asymmetrical models of the human lung. Implementation of the symmetrical model is relatively straightforward but the resulting predictions may not be entirely appropriate since the real airways do not branch symmetrically. More accurate predictions may be obtained with an asymmetrically branching airway network, such as the Horsefield model. Implementation of an asymmetrical model to predict input impedance is also rather straightforward but one to predict transfer impedance is very difficult. To solve the problems arising from modeling an asymmetrical tree structure, a superposition model was proposed based on the assumption that the system behaves linearly when small amplitude forced oscillations are applied. The tree structure of the airway was first horizontally divided into an asymmetrical zone and a symmetrical zone. The asymmetrical zone was further pruned into three subtrees. A uniquely indexed binary tree representation was developed from Horsefield's model using recursive algorithms applied to the asymmetrical zone to

compute the flow in all airway segments resulting from pressure sources at all alveoli, each considered separately. The sum of these flows was then calculated and the transfer impedance was computed straightforwardly from its definition.

A rat lung model was also implemented to aid in the design of experiments to determine sound exposure limits in humans.

2. Background

2.1. Symmetrical airway morphometry: Weibel's model of human lung and Yeh's model of rat lung

The treelike structure (Fig. 1) of the pulmonary airways can be analyzed in mathematical terms and related to its function [16]. Two commonly used human airway models are the Weibel's symmetrically branching tree structure [11] and the Horsefield's asymmetrically branching tree structure [12]. In the human lung model proposed by Weibel, the airways branch 24 times from the trachea (order 1) to the alveolar ducts (order 24). Each branch divides into two identical daughter branches. The lengths and diameters of the airways were determined by standard morphological techniques on five normal human lungs inflated to total lung capacity (TLC) [11]. All airways of a given order are assumed to have the same diameter and length. Thus, all pathways from the trachea to the alveoli are identical. The mean diameter and length of each airway order are listed in Table 1.

Table 1. Weibel's symmetrical model A of the human lung

Order n	Number per generation N	Diameter $d(n)$ cm	Length $l(n)$ cm
24	1	1.8	12
23	2	1.221	4.78
22	4	0.828	1.91
21	8	0.562	1.27
20	16	0.445	1.07
19	32	0.351	0.9
18	64	0.281	0.76
17	128	0.227	0.76
16	256	0.186	0.64
15	512	0.154	0.54
14	1024	0.13	0.46
13	2048	0.11	0.39
12	4096	0.095	0.33
11	8192	0.083	0.27
10	16384	0.073	0.23
9	32768	0.065	0.2
8	65536	0.059	0.16
7	131072	0.054	0.14
6	262144	0.05	0.12
5	524288	0.047	0.1
4	1048576	0.045	0.08
3	2097152	0.043	0.07
2	4194304	0.042	0.06
1	8388608	0.042	0.05

Unlike Weibel's model, the model of the rat lung proposed by Yeh et al [16] is a model without connectivity. Based on very complete anatomical data measured by Raabe et al., the number of terminal bronchioles (N_{tb}) was measured and the median number of generation (order) m down all the pathways to terminal bronchioles was calculated. The average branching ratio x was obtained from the equation $N_{tb} = x^{m-1}$, where x may not be an integer, which implies that the connectivity is undefined. This may also be called an "average-path" lung model. The average-path model of the airways in the rat lung is shown in Table 2. To be consistent with the numbering used in our Weibel model, order 24 in Table 2 represents the trachea, and generation 1 represents the terminal airway.

Table 2. Yeh's symmetrical model of rat lung

order n	Number per generation N	Diameter $d(n)$ cm	Length $l(n)$ cm
24	1	0.3400	2.6800
23	2	0.2900	0.7150
22	3	0.2630	0.4000
21	5	0.2030	0.1760
20	8	0.1630	0.2080
19	14	0.1340	0.1170
18	23	0.1230	0.1140
17	38	0.1120	0.1300
16	65	0.0950	0.0990
15	109	0.0870	0.0910
14	184	0.0780	0.0960
13	309	0.0700	0.0730
12	521	0.0580	0.0750
11	877	0.0490	0.0600
10	1477	0.0360	0.0550
9	2487	0.0200	0.0350
8	4974	0.0170	0.0290
7	9948	0.0160	0.0250
6	19896	0.0150	0.0220
5	39792	0.0140	0.0200
4	79584	0.0140	0.0190
3	159168	0.0140	0.0180
2	318336	0.0140	0.0170
1	636672	0.0140	0.0170

2.2. Asymmetrical airway morphometry: Horsefield's model of human lung

In the Horsefield model the airways are classified by the airway order n starting from the terminal airway (order 1) to the trachea (order 36) [12]. In this model, an airway of order n branches into two daughters of order $n-1$ and order $n-1-\Delta(n)$, where $\Delta(n)$ is the recursion index that characterizes the degree of asymmetry at each airway order. As one can see, connectivity in this model is defined. The model represents the average asymmetry found in the lung studied by Horsefield et al. The diameter $d(n)$, length $l(n)$, as well as a recursion index $\Delta(n)$ of each airway order are specified (Table 3).

Note that we have modified the diameters of the last eight orders since physiologically, it is unlikely to have increased diameters for lower orders. The new diameters were assumed to follow the diameter-generation relationship given by Weibel [11]:

$$d(n) = d_0 \cdot e^{-(0.293 - 0.00624 \cdot n) \cdot n}$$

where d_0 is diameter of 9th order in Horsefield's model which is the starting point of the fitting curve, and n is the generation number in Weibel's model.

The comparison of modified diameters and the original ones are shown in Fig. 3.
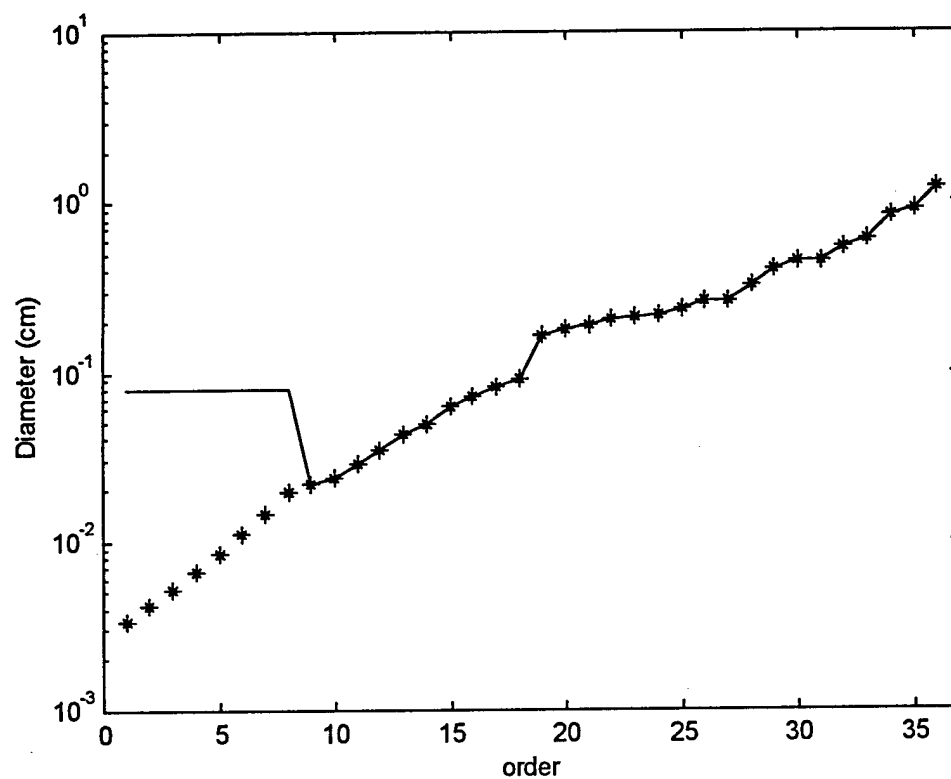
Figure 3. Diameters of Horsefield's model (-) and modified data (*) as a function

of order number.

Table 3. Horsefield's asymmetrical model of human lung

Order n	Number per order N	Delta $\Delta(n)$	Diameter $d(n)$ cm	Length $l(n)$ cm
36	1	1	1.6000	10.000
35	1	2	1.2000	5.000
34	2	3	1.1000	2.200
33	2	3	0.8000	1.100
32	3	3	0.7300	1.050
31	3	3	0.5900	1.130
30	5	3	0.5900	1.130
29	7	3	0.5400	0.970
28	10	3	0.4300	1.080
27	13	3	0.3500	0.950
26	18	3	0.3500	0.860
25	25	3	0.3100	0.990
24	35	3	0.2900	0.800
23	48	3	0.2800	0.920
22	66	3	0.2700	0.820
21	91	3	0.2500	0.810
20	126	3	0.2400	0.770
19	174	3	0.2180	0.640
18	240	3	0.2000	0.630
17	331	3	0.1800	0.517
16	457	3	0.1600	0.480
15	631	2	0.1400	0.420
14	871	2	0.1100	0.360
13	1202	1	0.0950	0.310
12	2290	0	0.0760	0.250
11	6653	0	0.0630	0.110
10	13306	0	0.0530	0.131
9	26612	0	0.0480	0.105
8	53224	0	0.0430	0.075
7	106448	0	0.0323	0.059
6	212896	0	0.0245	0.048
5	425792	0	0.0189	0.048
4	851584	0	0.0147	0.048
3	1703168	0	0.0116	0.048
2	3406336	0	0.0093	0.048
1	6812672	0	0.0075	0.048

3. Methods

3.1 Transfer function for single airway segment

3.1.1 Series impedance and shunt admittance of a nonrigid tube

The acoustical properties of an airway segment were modeled in terms of the series impedance composed of gas resistance (R_g) and inertance (I_g), and shunt admittance which is due to gas compression (C_g), thermal losses (G_g), and wall properties (Z_w) (Fig. 4) [3,15].
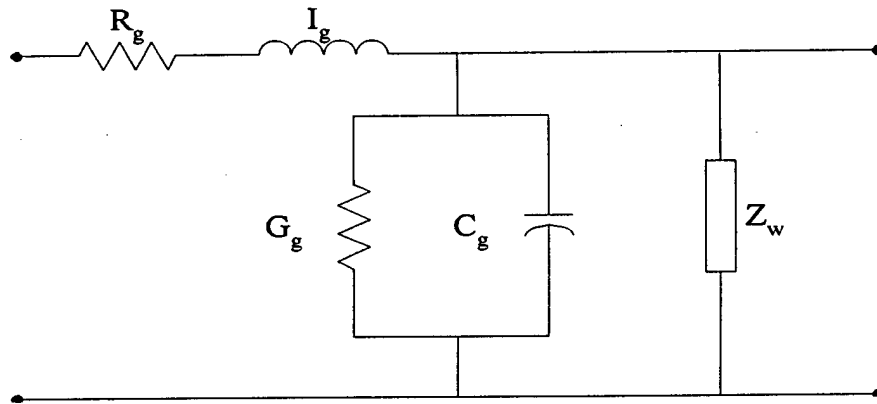
Figure 4. Transmission line representation of small segment of nonrigid tube

The series impedance $Z_{g,s}$ and shunt admittance ($Y_{g,p}+Y_w$) are defined as

$$Z_{g,s} = R_g + j\omega I_g \qquad (1)$$

$$Y_{g,p} + Y_w = G_g + j\omega C_g + Y_w \qquad (2)$$

where Y_w is wall admittance ($Y_w = 1/ Z_w$). The coupling of $Z_{g,s}$ and shunt admittance determines the characteristic impedance Z_0 and propagation coefficient γ given as

$$Z_0 = \sqrt{\frac{Z_{g,s}}{Y_{g,p} + Y_w}} \qquad (3)$$

$$\gamma = \sqrt{Z_{g,s} \cdot (Y_{g,p} + Y_w)} = \alpha + j\beta \qquad (4)$$

where α is the attenuation coefficient determining the amount of exponential attenuation of the wave amplitude along the airway segment; and β is the measure of phase change of the wave. The wave propagation velocity c and β are related by

$$c = \frac{\omega}{\beta} \qquad (5)$$

where $\omega = 2\pi f$, f is frequency in Hz.

3.1.2 Transmission line theory and two-port network representation

Each segment of the airway, which is the basic computational unit of the proposed model, can be modeled as a two-port (four-terminal) network as illustrated in Fig. 5.

14
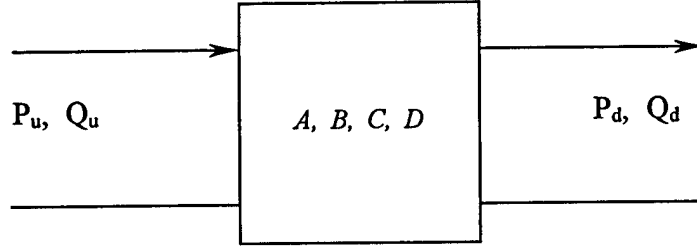
Figure 5. Four-terminal network representation of a segment of airway

The pressure drop and flow discharge of the segment based on transmission line theory are given by [10]

$$P_u = P_d \cosh(\gamma l) + Q_d Z_0 \sinh(\gamma l) \tag{6}$$

$$Q_u = P_d \frac{\sinh(\gamma l)}{Z_0} + Q_d \cosh(\gamma l) \tag{7}$$

where P_u and P_d are the upstream and downstream pressure (in cmH_2O), respectively. Q_u and Q_d are the upstream and downstream flow (in L/s), respectively. And l is the length of the airway segment (in cm). The characteristic impedance Z_0 and propagation coefficient γ are obtained from Eq. (3) and (4).

The transmission matrix (T-parameter) for the network in Fig. 5 can be derived from Eq. (6) and Eq. (7) as

$$\begin{bmatrix} P_u \\ Q_u \end{bmatrix} = \begin{bmatrix} A & B \\ C & D \end{bmatrix} \begin{bmatrix} P_d \\ Q_d \end{bmatrix} \tag{8}$$

where

$$A = \cosh(\gamma l) \tag{9}$$

$$B = Z_0 \sinh(\gamma l) \tag{10}$$

$$C = \frac{\sinh(\gamma l)}{Z_0} \tag{11}$$

$$D = \cosh(\gamma l) \tag{12}$$

In the implementation of the model, these airway segments (equivalent networks) are connected either in series or in parallel. Connecting segments in series is conveniently done by multiplying T-matrices of all the network blocks. However, connecting segments in parallel is more conveniently accomplished by adding their admittances, Y-parameters, defined by

$$\begin{bmatrix} Q_u \\ Q_d \end{bmatrix} = \begin{bmatrix} y_{11} & y_{12} \\ y_{21} & y_{22} \end{bmatrix} \begin{bmatrix} P_u \\ P_d \end{bmatrix} = \begin{bmatrix} \dfrac{\cosh(\gamma l)}{Z_0 \sinh(\gamma l)} & -\dfrac{1}{Z_0 \sinh(\gamma l)} \\ -\dfrac{1}{Z_0 \sinh(\gamma l)} & \dfrac{\cosh(\gamma l)}{Z_0 \sinh(\gamma l)} \end{bmatrix} \begin{bmatrix} Q_u \\ Q_d \end{bmatrix} \tag{13}$$

3.1.3. Model of airway wall properties and tissue properties

The measurement of wave propagation velocity in dog tracheae made by Guelke and Bunn [21] indicated that it was frequency dependent which implicates that the airway is not rigid. A single compartment model including resistive, inertive, and elastic elements

was used to explain this frequency dependence. Later, Suki et al. [15] found a more complex frequency dependence of propagation velocity in excised calf tracheae which led to a two-compartment representation of wall properties [15]. As suggested by their study, a two-compartment model is used to model soft tissue and cartilage in the airway walls with diameters greater than 2 *mm* (Fig. 6). The walls of airways whose diameter is less than 2 *mm* are modeled with a single soft tissue compartment due to the absence of cartilage.
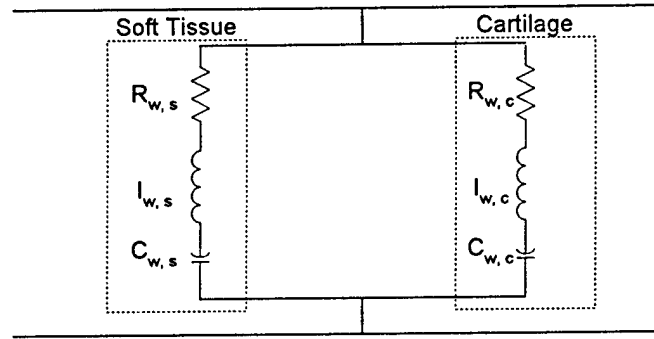
Figure 6. Two compartment model of airway wall properties

The volumetric properties of the airway walls are computed from equations derived by Suki et al. [15] and given below. The resistance is given by

$$R_{w(n)} = \frac{4h(n)v}{\pi d^3(n)l(n)} \tag{14}$$

where *d(n)*, *l(n)*, and *h(n)* are airway segment diameter, length and wall thickness, respectively; and v is viscosity of either cartilage or soft tissue. The inertance is given by

$$I_{w(n)} = \frac{h(n)\rho}{\pi d(n)l(n)} \tag{15}$$

where ρ is density of the tissue (either cartilage or soft tissue). Finally, the capacitance is given by

$$C_{w(n)} = \frac{\pi d^3(n)l(n)}{4h(n)Y} \qquad (16)$$

where Y is Young's modulus of either cartilage or soft tissue.

The densities of the cartilage and soft tissue (ρ_c and ρ_s) were fixed to 1.14 and 1.06 g/ml, respectively [1]. The Young's modulus for cartilage (Y_c) was fixed to the mean value (4000 cmH$_2$O) reported in human tracheal cartilage stripes [19]. The soft tissue viscosity ν_s and the Young's modulus Y_s were fixed to the mean values of 1.04 cmH$_2$O and 593 cmH$_2$O respectively, which were reported by Habib et al. [1]. Based on the empirical findings of Suki et al. [15], it was assumed that cartilage and soft tissue have comparable viscosity-to-elasticity ratios; i.e., $\nu_s/Y_s = \nu_c/Y_c$. Therefore, the cartilage viscosity ν_c was fixed to a value of (7.015 cmH$_2$O) calculated from this formula.

The cartilage content $c(n)$ is a function of $d(n)$ as proposed by Gunst and Stropp [15]:

$$c(n) = -0.09d^2(n) + 0.25d(n) - 0.024 \qquad (17)$$

Since the soft tissue content is simply $1-c(n)$, the effective wall volumetric impedance $Z_{w,eff}$ of an airway segment of order n is

$$Z_{w,\,eff}(n) = \frac{Z_{w,\,c}(n) \cdot Z_{w,\,s}(n)}{c(n) \cdot Z_{w,\,s}(n) + [1 - c(n)] \cdot Z_{w,\,c}(n)} \qquad (18)$$

where $Z_{w,c}$ and $Z_{w,s}$ represent cartilage and soft tissue compartment impedances, respectively.

The wall thickness is required to compute the volumetric properties of the airway wall (Eqns. 14 – Eq. 16). Habib et al. [1] used a polynomial expression approximating the data of the wall area internal to the smooth muscle layer $WA_{sm}(n)$ as a function of internal airway perimeter $\pi d(n)$ for healthy human lungs from Wiggs et al. [15]. By assuming a circular geometry for both the luminal and external wall surfaces, the wall thickness internal to the outer smooth muscle layer $h_{sm}(n)$ was computed as a function of internal diameter $d(n)$ as [1]

$$h_{sm}(n) = \sqrt{d^2(n)/4 + WA_{sm}(n)/\pi} - d(n)/2 \qquad (19)$$

Furthermore, in order to obtain the thickness of the entire airway wall (not only smooth muscle layer), Habib et al. applied system identification methods to estimate the total wall thickness as a function of the diameter of a given generation. In the current study, the airway thickness data of Habib et al. are used for our Horsefield-based, asymmetrical human lung model. The thickness of the airway walls in our Weibel-based, symmetrical human model and our Yeh-based rat lung model were predicted from a polynomial fit of thickness as a function of airway order published by Habib et al. [1] (Fig. 7).
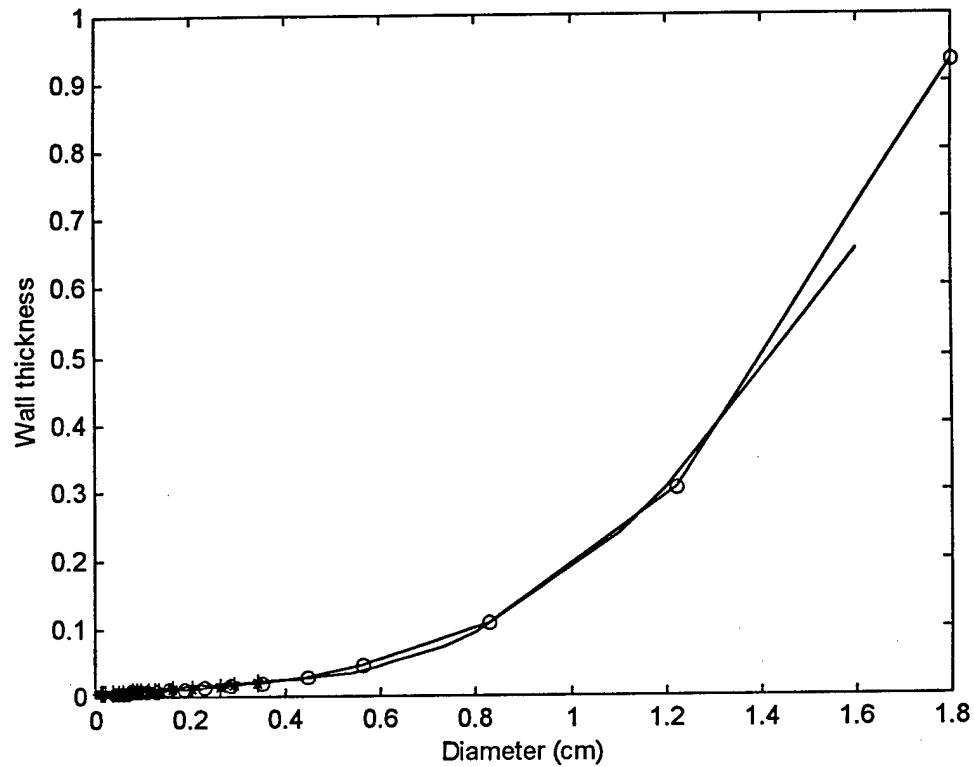
Figure. 7. Polynomial fit of wall thickness data from Habib et al.

The wall thickness and cartilage content data are listed in Table 4, Table 5, and Table 6, for the Horsefield's human lung model, the Weibel's human lung model, and the Yeh's rat lung model, respectively.

Table 4. Airway wall parameters based on diameters of the Horsefield's model

Order n	Wall thickness h(n) cm	Cartilage Content c(n)
36	0.6554	0.6700
35	0.3054	0.5000
34	0.2372	0.5000
33	0.0929	0.3300
32	0.0720	0.2500
31	0.0429	0.2000
30	0.0429	0.0926
29	0.0361	0.0851
28	0.0262	0.0671
27	0.0222	0.0526
26	0.0222	0.0526
25	0.0208	0.0450
24	0.0201	0.0410
23	0.0197	0.0390
22	0.0195	0.0370
21	0.0188	0.0329
20	0.0185	0.0309
19	0.0176	0.0262
18	0.0169	0.0224
17	0.0160	0
16	0.0150	0
15	0.0139	0
14	0.0118	0
13	0.0106	0
12	0.0088	0
11	0.0074	0
10	0.0063	0
9	0.0056	0
8	0.0051	0
7	0.0038	0
6	0.0029	0
5	0.0022	0
4	0.0017	0
3	0.0014	0
2	0.0011	0
1	0.0009	0

Table 5. Wall parameters for Weibel's model.

Order n	h(n)	c(n)
24	0.9321	0.1344
23	0.3059	0.1471
22	0.1094	0.1213
21	0.0460	0.0881
20	0.0303	0.0694
19	0.0215	0.0527
18	0.0167	0.0391
17	0.0137	0.0281
16	0.0118	0.0194
15	0.0104	0.0124
14	0.0095	0.0070
13	0.0087	0.0024
12	0.0082	0
11	0.0077	0
10	0.0074	0
9	0.0071	0
8	0.0069	0
7	0.0067	0
6	0.0066	0
5	0.0064	0
4	0.0064	0
3	0.0063	0
2	0.0063	0
1	0.0063	0

Table 6. Wall parameters for Yeh's model.

Order n	h(n)	c(n)
24	0.0117	0.0506
23	0.0098	0.0409
22	0.0089	0.0355
21	0.0071	0.0230
20	0.0061	0.0144
19	0.0055	0.0079
18	0.0052	0.0054
17	0.0050	0.0029
16	0.0046	0
15	0.0045	0
14	0.0043	0
13	0.0041	0
12	0.0039	0
11	0.0037	0
10	0.0034	0
9	0.0031	0
8	0.0031	0
7	0.0030	0
6	0.0030	0
5	0.0030	0
4	0.0030	0
3	0.0030	0
2	0.0030	0
1	0.0030	0

The most peripheral airways were assumed to be uniformly terminated by a single alveolar sac (Fig. 8). The terminal parenchymal and chest wall tissues are modeled as series resistance-inertance-capacitance tissue impedance in parallel with a capacitance due to alveolar gas compression [1, 5] (Fig. 9).
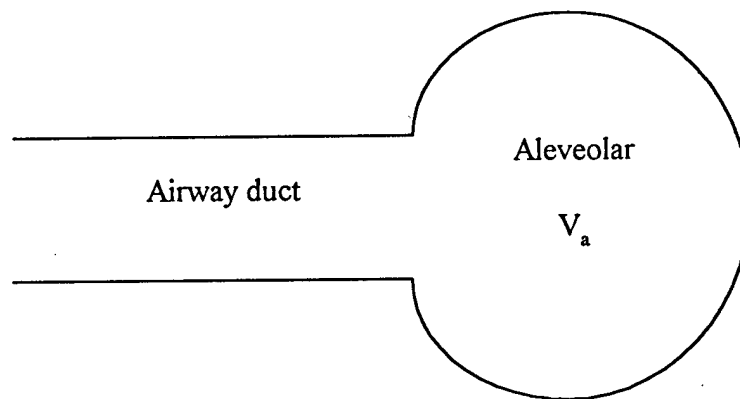
Figure 8. The most peripheral airway terminated by a single alveolar sac.
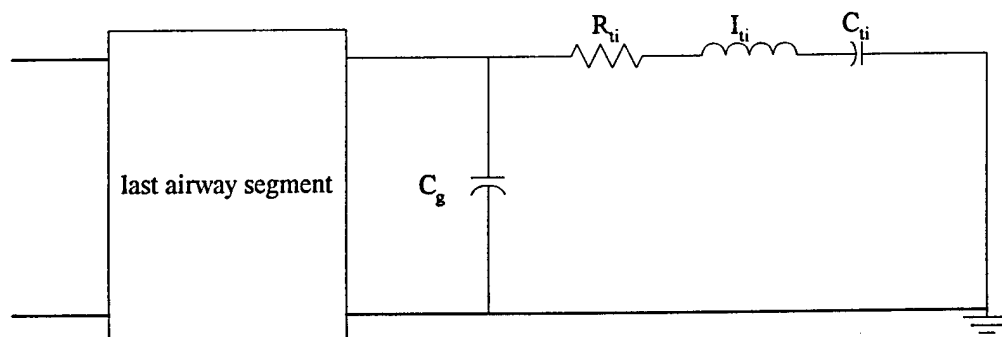
Figure 9. Model of tissue properties and alveolar gas compression.

The parameters (R_{ti}, I_{ti}, and C_{ti}) of tissue properties of both human lung models were taken from Peslin et al. [8]. The rat lung tissue properties were assigned the values published by Jackson et al. [23]. The alveolar gas compression compliance C_g was calculated with the assumption of isothermal conditions from assigned lung volume V_L (usually takes the value of functional residual capacity FRC) and mean pressure. The gas volume in a single alveolar sac is $\frac{V_L}{N}$, where N is the total number of terminal airways. The partial pressure of the compressible 100% humidified gas in the alveoli was assumed to be P_{atm}-P_{H2O}, where P_{atm} is atmospheric pressure (1033 cmH_2O) and P_{H2O} is the partial pressure of water vapor at 100% saturation (64 cmH_2O) [4]. Thus, C_g is

$$C_g = \frac{V_L}{N \cdot \left(P_{atm} - P_{H2O}\right)} \tag{20}$$

Using dimensions (cross-sectional area versus distance from the airway opening) of the oral and oral pharyngeal cavities (Dan Olsen, unpublished measurements) we approximated the geometry of the upper airways as 6-segments whose lengths and diameters are given in Table 9, where the wall thickness was computed from Eq. 19. Habib provided evidence that the upper airways in the human lung behave as a two compartment model whose lumped properties are given in Table 8 [26]. We know of no data by which we could assign separate values to the 6 separate segments of our model. Therefore we simply assumed that those airway wall properties suggested by Habib were distributed uniformly along the upper airways. Order 1 is the segment next to trachea and order 6 is the uppermost one.

Table 7. Structural parameters of the upper airways of the human airway model

Order n	Diameter d(n) (cm)	Length l(n) (cm)	Thickness h(n) (cm)
6	4.4000	2.7500	1.8000
5	4.9000	2.7500	1.8000
4	4.4000	2.7500	1.8000
3	3.5000	4.4500	1.8000
2	3.0000	5.0000	3.4000
1	2.2000	5.5000	3.4000

Table 8. Lumped upper airway wall parameters from two-compartment model

Subject No.	R_{ch} $CmH_2O \cdot s$	I_{ch} $CmH_2O \cdot s$	C_{ch} L/CmH_2	R_{sm} $CmH_2O \cdot s/L$	k
1	14.5	0.0173	0.0009	1.7	1.18
2	75.8	0.0195	0.0020	10.9	1.7
3	9.7	0.0197	0.0009	33.1	2.23
4	33.0	0.0343	0.0005	21.0	2.75
5	56.9	0.0104	0.0014	9.5	3.53
Mean	38.0	0.0202	0.0011	15.2	2.28
±SD	±25.2	0.0078	0.0005	10.8	0.82

The excised lung used in Weibel's study was fixed to 2400-ml [18]. It was assumed that the lung expansion was isotropic and the diameters were scaled linearly (i.e., 70%) [24]. Airways were assumed to be filled with alveolar gas, i.e. 100% humidified room air.

3.2 Input impedance and transfer impedance for symmetrically branching tree structure

3.2.1 Structure simplification

Consider the symmetrically branched tree structure (Fig. 10). The basic computational unit of the proposed model is a segment of airway, which is modeled as a two-port (four-terminal) network as discussed in section 3.1. Hence the entire tree-structured airway can be modeled as a network illustrated in Fig. 11.
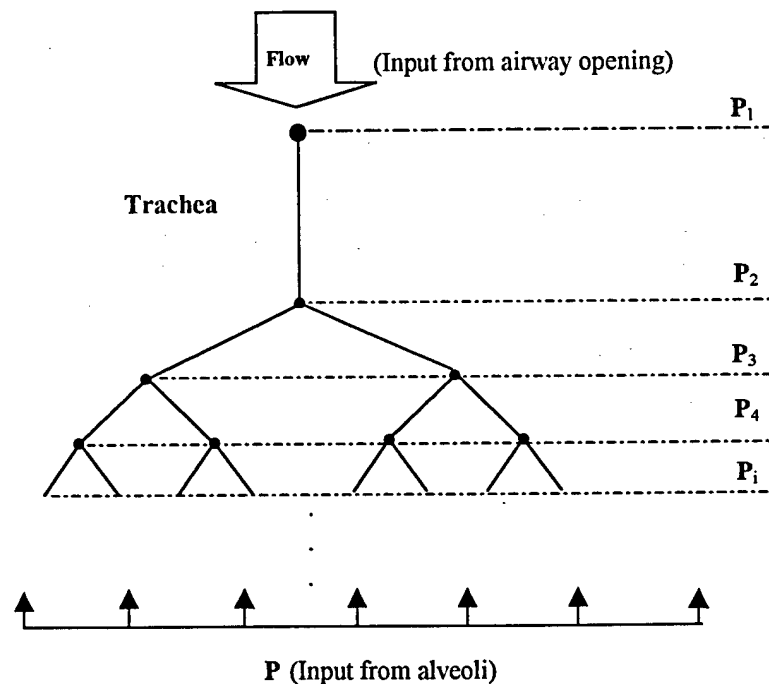
Figure 10. Symmetrical airway tree structure with input imposed at airway opening (single flow source) OR input imposed at alveoli (multiple pressure sources)
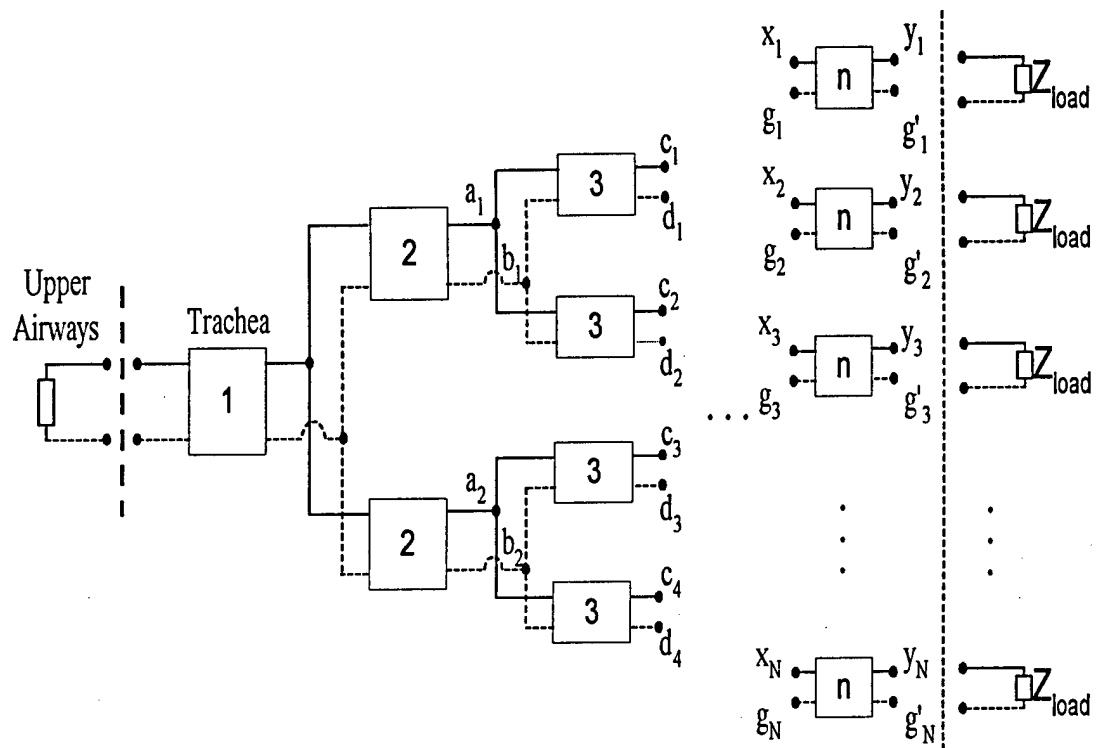
Figure 11. Two-port network representation of the symmetrical tree structure

The pressure drops across all airway segments of a given generation are identical, since the impedances of all segments are identical (Fig. 11). Hence, the pressures at points a_1 and a_2 are the same, and pressures at points b_1 and b_2 are the same as well. For the same reason, the pressures at points c_1-c_4 are identical and the pressures at points d_1-d_4 are also identical. By connecting these equal-pressure points, the simplified network structure is obtained as shown in Fig. 12 [13].
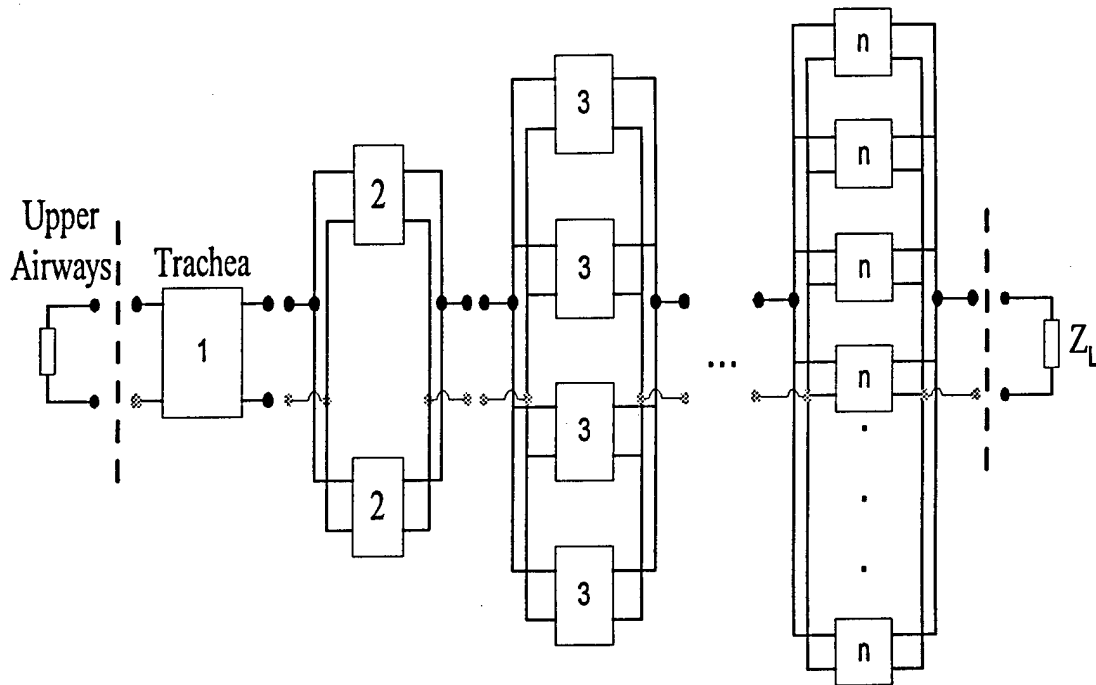
Figure 12. Simplified network structure. The dichotomous branching pattern turned into simpler parallel connection of two-port network blocks for the corresponding airway segments.

The structure in Fig. 12 can be further simplified by substituting an equivalent two-port network for each airway generation, namely, collapsing all the network blocks into a single equivalent two-port network block with the algorithm described in section 3.1.2. The further simplified series two-port network structure is shown in Fig. 13.
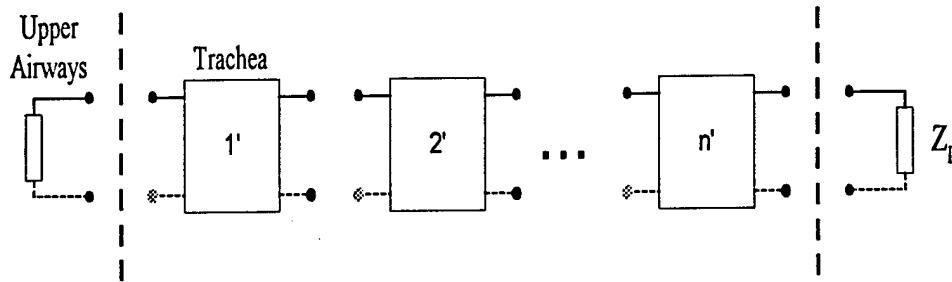
Figure 13. Series two-port network equivalent model of symmetrical airway tree structure.

3.2.2 Algorithm for computing the equivalent T-parameters of parallel network connection

The Y and T parameters of one two-port network block of a given generation can be obtained as described in section 3.1.2. The equivalent Y parameter matrix Y_p of m blocks connected in parallel as shown in Fig. 14 is [17]

$$Y_p = \sum_{i=1}^{m} Y_i \qquad (21)$$

where Yi is the Y matrix of ith network block, $i=1, 2, \ldots m$.
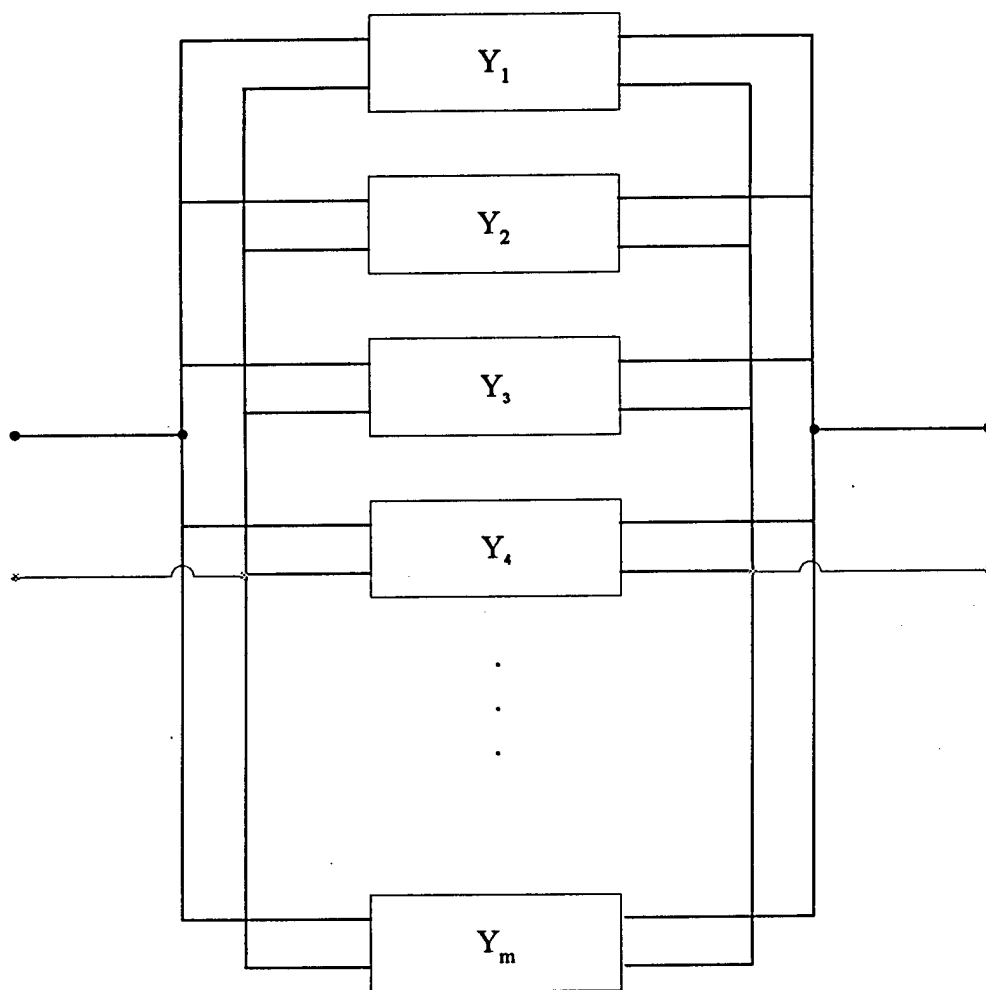
Figure 14. *m* two-port network are connected in parallel

For m identical network blocks, where $Y_i=Y$ for $i=1, 2, \ldots m$, the parameters of the equivalent Y_p-matrix are simply the product of m and the corresponding parameters in the Y-matrix:

$$Y_p = m \cdot Y = \begin{bmatrix} m \cdot y_{11} & m \cdot y_{12} \\ m \cdot y_{21} & m \cdot y_{22} \end{bmatrix} \tag{22}$$

The T parameters expressed in terms of the Y-parameters are (see details in Appendix A)

$$T = \begin{bmatrix} t_{11} & t_{12} \\ t_{21} & t_{22} \end{bmatrix} = \begin{bmatrix} -\dfrac{y_{22}}{y_{21}} & -\dfrac{1}{y_{21}} \\ -\dfrac{\Delta y}{y_{21}} & -\dfrac{y_{11}}{y_{21}} \end{bmatrix} \tag{23}$$

where Δy is the determinant of the Y matrix. The determinant of the Y_P-matrix expressed in terms of the Y-matrix is

$$\Delta_{Y_p} = m^2 \cdot \Delta_Y \tag{24}$$

Therefore, T_p can be derived in terms of the T-parameters from Eq. (22) and Eq. (23) as follows:

$$T_P = \begin{bmatrix} -\dfrac{m \cdot y_{22}}{m \cdot y_{21}} & -\dfrac{1}{m \cdot y_{21}} \\ -\dfrac{m^2 \cdot \Delta y}{m \cdot y_{21}} & -\dfrac{m \cdot y_{11}}{m \cdot y_{21}} \end{bmatrix} = \begin{bmatrix} t_{11} & \dfrac{t_{12}}{m} \\ m \cdot t_{21} & t_{22} \end{bmatrix} \tag{25}$$

32

Thus, even for parallel connections of the network, we do not have to compute the Y-parameters. Only the T-parameters are needed to compute impedance of individual airway segments and equivalent networks of parallel connections of these segments.

In Weibel's model of the human lung, m of a given generation is $m=2^n$, where n is the generation number. In the Yeh's model of the rat lung, m is calculated based on the average branching ratio (which is not 2, and sometimes, is not even an integer) of the given generation as listed in Table 2. Here, it can be noticed that m is not two to the power of the generation number n.

3.2.3 Algorithm for computing the equivalent T parameters of series network connections

After obtaining the T_p's for all generations, the next task was to compute the equivalent T parameter matrix, T_s, of the series network connection (Fig. 15) in order to get a single equivalent network.
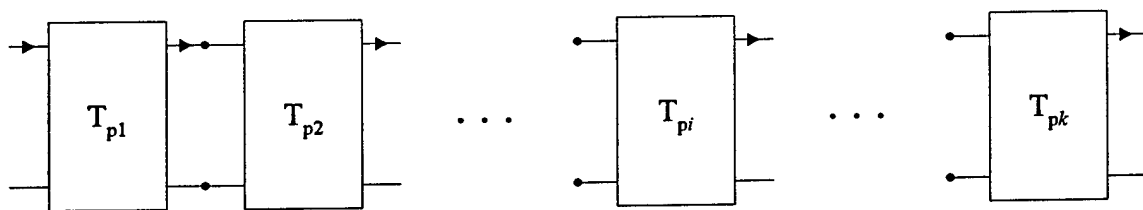
Figure 15. Series connection of k two-port network blocks

The equivalent T-parameter matrix Ts of k network blocks connected in series as shown in Fig. 15 is [17]

$$T_s = \prod_{i=1}^{k} T_{pi}$$ (26)

This can be realized using the following recursive algorithm:

Initialize T_s as a 2x2 unity matrix.

for i=1 to k

$$T_s = T_s * T_{pi}$$

end

The resulting single two-port network block is shown in Fig. 16.
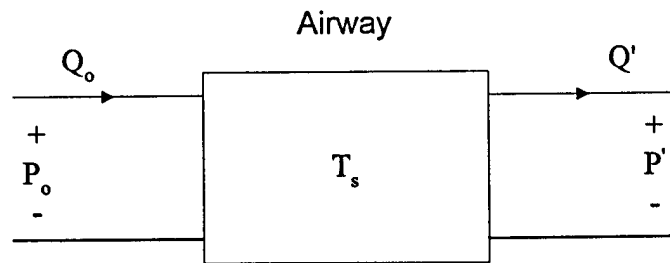
Figure 16. Single two-port network equivalent of airway tree structure

3.2.4 Input and transfer impedances

The model for the entire respiratory system (Fig. 17) is obtained by combining the airway and tissue properties.
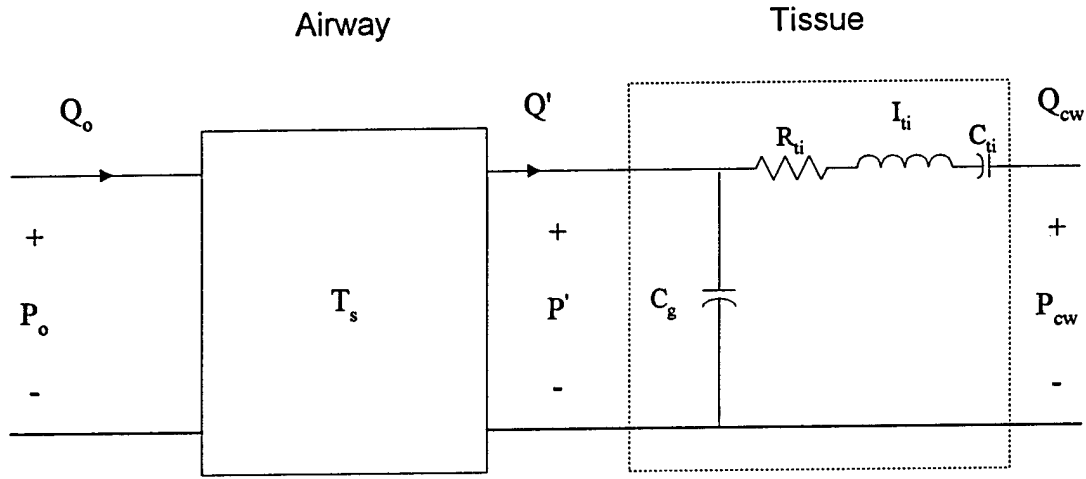
Figure 17. Integrated respiratory system model

For Zin computations, the impedance of the chest wall and tissues, Rti-Iti-Cti in series, which is placed in parallel with alveolar gas compression capacitance, can be considered as the load impedance of the airway two–port network (Fig. 17). Thus Zin looking from the trachea is computed as

$$Z_{in} = \frac{t_{s11} \cdot Z_{load} + t_{s12}}{t_{s21} \cdot Z_{load} + t_{s22}} \qquad (27)$$

where t_{s11}, t_{s12}, t_{s21}, and t_{s22} are the four parameters in T_s matrix ; and Z_{load} is

$$Z_{load} = \frac{Z_{ti} \cdot Z_g}{Z_{ti} + Z_g} \qquad (28)$$

where

$$Z_{ti} = \frac{(R_{ti} + j\omega I_{ti} + \dfrac{1}{j\omega C_{ti}})}{N_{endings}} \qquad (29)$$

$$Z_g = (j\omega C_g) \cdot N_{ends} \qquad (30)$$
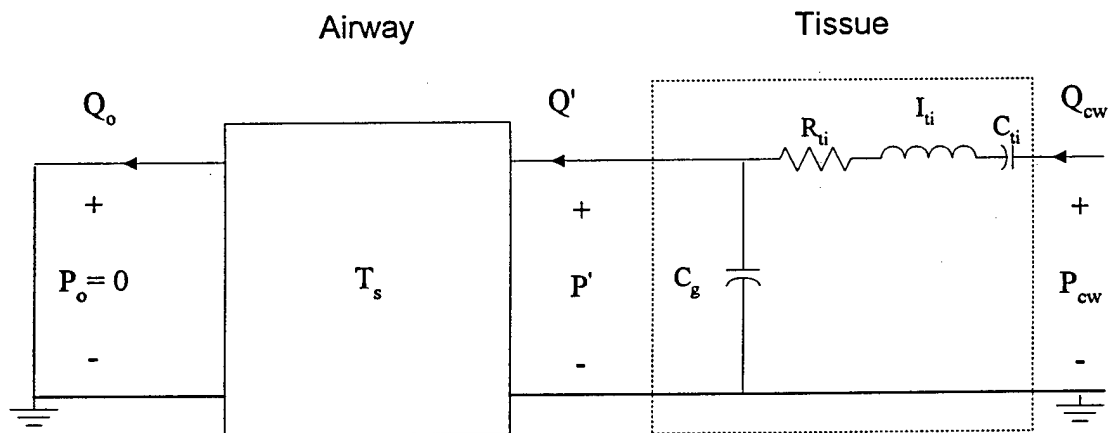
Figure 18. Integrated network model for transfer impedance

For Ztr (Fig. 18), the T-parameters of the two-port network of tissue properties and gas compression can be derived from linear circuit analysis (see details in Appendix A):

$$\begin{bmatrix} P_{cw} \\ Q_{cw} \end{bmatrix} = T_{ti} \cdot \begin{bmatrix} P' \\ Q' \end{bmatrix} = \begin{bmatrix} 1 + \dfrac{Z_{ti}}{Z_g} & Z_{ti} \\ \dfrac{1}{Z_g} & 1 \end{bmatrix} \cdot \begin{bmatrix} P' \\ Q' \end{bmatrix} \quad (31)$$

It may be noticed that T_s (Fig. 17) is the transmission matrix from trachea to alveoli. The transmission matrix from the alveoli towards the trachea, T_{cw_o}, can be expressed in terms of the parameters in the matrix T_s as

$$\begin{bmatrix} P' \\ Q' \end{bmatrix} = T_{cw\_o} \cdot \begin{bmatrix} P_o \\ Q_o \end{bmatrix} = \begin{bmatrix} t_{s22} & t_{s12} \\ t_{s21} & t_{s11} \end{bmatrix} \cdot \begin{bmatrix} P_o \\ Q_o \end{bmatrix} \quad (32)$$

Therefore, the complete transmission matrix from alveoli to trachea is

$$\begin{bmatrix} P_{cw} \\ Q_{cw} \end{bmatrix} = T_{ti} \cdot T_{cw\_o} \cdot \begin{bmatrix} P_o \\ Q_o \end{bmatrix} \quad (33)$$

Combining Eqns 31 and 33, we have

$$\begin{bmatrix} P_{cw} \\ Q_{cw} \end{bmatrix} = T_{ti} \cdot T_{cw\_o} \cdot \begin{bmatrix} P_o \\ Q_o \end{bmatrix}$$

$$= \begin{bmatrix} 1 + \dfrac{Z_{ti}}{Z_g} & Z_{ti} \\ \dfrac{1}{Z_g} & 1 \end{bmatrix} \cdot \begin{bmatrix} t_{s22} & t_{s12} \\ t_{s21} & t_{s11} \end{bmatrix} \cdot \begin{bmatrix} P_o \\ Q_o \end{bmatrix}$$

$$= \begin{bmatrix} (1 + \dfrac{Z_{ti}}{Z_g}) \cdot t_{s22} + Z_{ti} \cdot t_{s21} & (1 + \dfrac{Z_{ti}}{Z_g}) \cdot t_{s12} + Z_{ti} \cdot t_{s11} \\ \dfrac{t_{s22}}{Z_g} + t_{s21} & \dfrac{t_{s12}}{Z_g} + t_{s11} \end{bmatrix} \cdot \begin{bmatrix} P_o \\ Q_o \end{bmatrix} \qquad (34)$$

The transfer impedance Ztr is thus given by

$$Z_{tr} = \frac{P_{cw}}{Q_o}\Big|_{P_o=0} = (1 + \frac{Z_{ti}}{Z_g}) \cdot t_{s12} + Z_{ti} \cdot t_{s11} \qquad (35)$$

3.2.5 Pressure ratios

The ratios of the pressure at the ends of airway branches of a given generation, divided by the applied pressure can be computed using the same scheme. In general, the airway opening is terminated by a load impedance, Z_L (Fig .19).

Z_{in} at the end of each stage is the load impedance of the next stage. For example, $Z_{in}(1)$ in Fig .19 is

$$Z_{in1}(1) = \frac{t_{p11}(1) \cdot Z_L + t_{p12}(1)}{t_{p21}(1) \cdot Z_L + t_{p22}(1)} \qquad (36)$$

where $t_{p11}(1)$, $t_{p12}(1)$, $t_{p21}(1)$, and $t_{p22}(1)$, are parameters in the transmission matrix T_{p1} obtained in section 3.2.2.

Z_{in} of the next stage, $Z_{in}(2)$ is

$$Z_{in}(2) = \frac{t_{p11}(2) \cdot Z_{in}(1) + t_{p12}(2)}{t_{p21}(2) \cdot Z_{in}(1) + t_{p22}(2)} \tag{37}$$

where $t_{p11}(2)$, $t_{p12}(2)$, $t_{p21}(2)$, and $t_{p22}(2)$ are parameters in the transmission matrix T_{p2}.

This is also a recursive process. Therefore, the input impedances, $Z_{in}(i)$, i=1, 2, ..., k can be computed using a recursive algorithm:

$$Z_{in}(i) = \frac{t_{p11}(i) \cdot Z_{in}(i-1) + t_{p12}(i)}{t_{p21}(i) \cdot Z_{in}(i-1) + t_{p22}(i)} \tag{38}$$

where $t_{p11}(i)$, $t_{p12}(i)$, $t_{p21}(i)$, and $t_{p22}(i)$ are parameters in i^{th} transmission matrix T_{pi} *for* i^{th} generation :

$$T_{pi} = \begin{bmatrix} \cosh(\gamma(i) \cdot l(i)) & \dfrac{Z_0(i) \cdot \sinh(\gamma(i) \cdot l(i))}{m(i)} \\ \dfrac{m(i) \cdot \sinh(\gamma(i) \cdot l(i))}{Z_0(i)} & \cosh(\gamma(i) \cdot l(i)) \end{bmatrix} \tag{39}$$

where $m(i)$ is the total number of airway segments of the ith generation, $l(i)$ is the length, $\gamma(i)$ is the propagation coefficient, and Z_0 is the characteristic impedance.
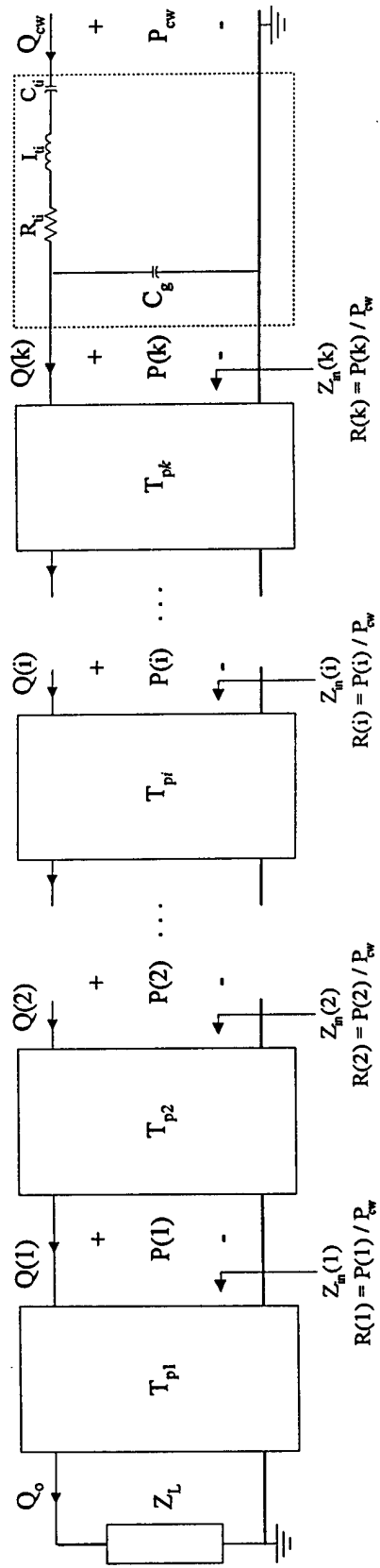
Figure 19. Pressure ratios when load impedance Z_L is in presence at the airway opening

40

Letting Pcw=1, the pressure ratio at each generation is equal to the pressure at the

corresponding generation, namely, $R(i) = \dfrac{P(i)}{P_{cw}} = P(i)$. Multiplying both sides of Eq. (31)

with the inverse of T_{ti}, we have:

$$
\begin{bmatrix} P(k) \\ Q(k) \end{bmatrix} = \begin{bmatrix} 1 & -Z_{ti} \\ -\dfrac{1}{Z_g} & 1+\dfrac{Z_{ti}}{Z_g} \end{bmatrix} \cdot \begin{bmatrix} P_{cw} \\ Q_{cw} \end{bmatrix} \tag{40}
$$

where P(k) and Q(k) correspond to P' and Q' in Eq. (31), respectively. The pressure P(k)

is

$$
P(k) = P_{cw} - Z_{ti} \cdot Q_{cw} = 1 - Z_{ti} \cdot Q_{cw} \tag{41}
$$

where Q_{cw} is computed as 1 divided by Z_{in_cw} since Pcw=1; and Z_{in_cw} is

$$
Z_{in\_cw} = \frac{(1+\dfrac{Z_{ti}}{Z_g}) \cdot Z_{in}(k) + Z_{ti}}{\dfrac{Z_{in}(k)}{Z_g} + 1} \tag{42}
$$

In general, the pressure at generation i can be calculated using the recursive

algorithm:

$$
P(i) = t_{p11}(i+1) \cdot P(i+1) - T_{p12}(i+1) \cdot \frac{P(i+1)}{Z_{in}(i+1)} \tag{43}
$$

Load impedance Z_L is zero when the mouth is open and approaches infinity when the

mouth is closed.

3.3 Input and transfer impedance for asymmetrically branching tree structure

3.3.1 Self-similarity algorithm for calculating input impedance Z_{in}

Z_{in} of the asymmetrical model is computed using self-similarity algorithms [1, 15]. It starts with the most peripheral airway and marches up the longest pathway to the airway opening using,

$$Z_{in}(n) = \frac{Z_T + Z_0 \tanh(\gamma l(n))}{1 + (Z_T / Z_0) \tanh(\gamma l(n))} \tag{44}$$

where Z_T is the parallel combination of the two daughter branches of order n,

$$Z_T = Z_{in}(n - 1) \,/\!/\, Z_{in}(n - 1 - \Delta(n)) \tag{45}$$

When n=1 (terminal airway), Z_T is the load impedance of the series tissue impedance in parallel with alveolar gas compression capacitance as described in Eq. (28).

3.3.2 Principle of superposition

Fluid mechanics in the airways due to small amplitude oscillations are considered to behave linearly and thus obey the superposition theorem. The superposition theorem says that [2]:

In any linear network containing several sources, the voltage (analogous to pressure) across or the current (analogous to flow) through any branch can be calculated by adding algebraically all the individual voltages or currents caused by each independent source acting alone, with

all other independent voltage sources replaced by short circuits and all the

other independent current sources replaced by an open circuit.

Let us first consider applying the pressure sources to the terminal airways of the simple tree network in Fig. 20. The flow due to a pressure applied to the 1st terminal airway alone (with pressure sources at 2nd and 3rd terminals grounded) is *Flow$_1$*. The flow due to a pressure applied to the 2nd terminal alone is *Flow$_2$*, and the flow due to a pressure applied to 3rd terminal alone is *Flow$_3$*. According to the superposition theorem, the total flow in each of the airway segments due to pressure sources simultaneously applied to all of the terminal airways is simply the sum of *Flow$_1$*, *Flow$_2$*, and *Flow$_3$*. Z_{tr} of the whole network, where all pressure sources, P, are identical, is:

$$Z_{tr} = \frac{P}{\sum Flow_k} \qquad (46)$$
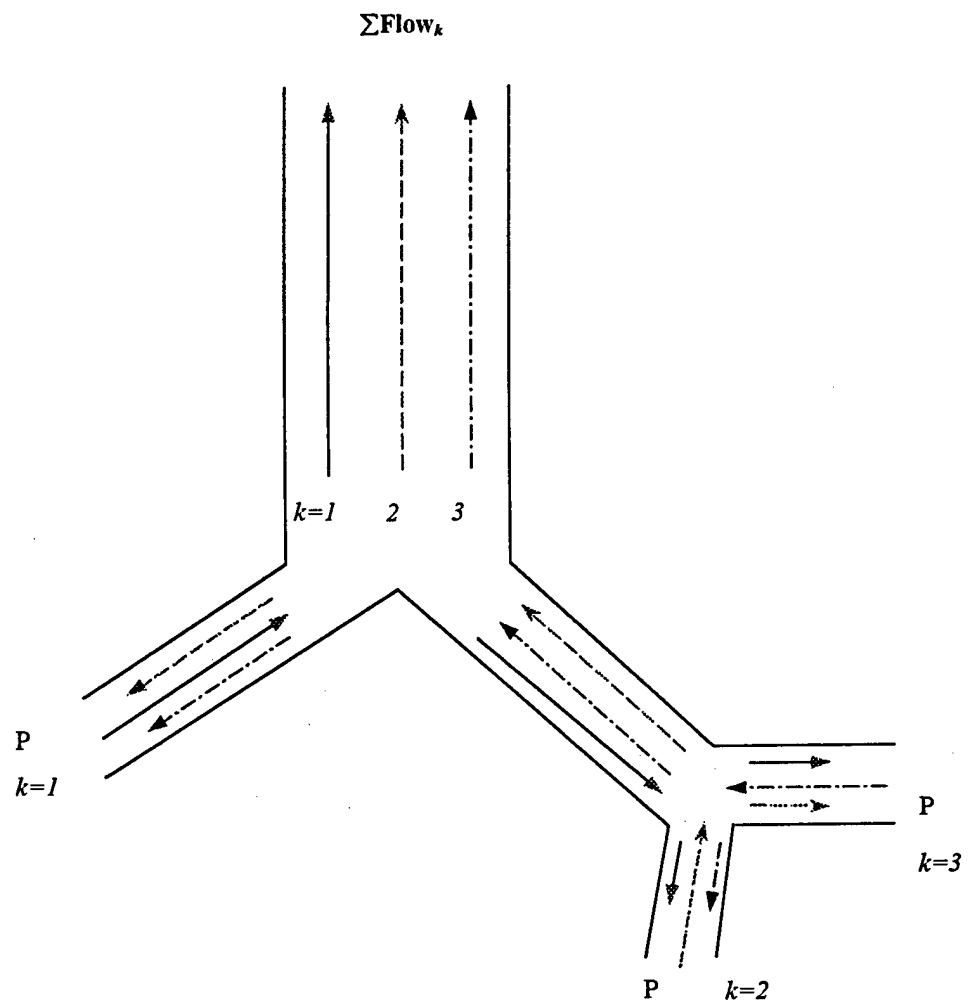
Figure 20. Superposition model of pressure-flow relationship

The superposition theorem enables us to compute Ztr by considering each single pressure source one by one. That is, it is not necessary to consider the network connection globally as we did to analyze Ztr in the symmetrical tree structure.

If the input impedances looking from bottom up along an airway path are available, it is quite straightforward to compute flows entering all the airway segments on this path. The output pressure of this segment can be calculated from the two-port network parameters, which are the input pressure of its parent. Therefore, marching up the path with this recursive process, we can obtain the flow due to the pressure applied at the bottom of this path. The remaining question is, how do we calculate input impedances looking up from the end of all the airway segments?

3.3.3 Analysis of the structure of Horsefield's model

Generally, from each different terminal airway, a different tree structure is seen. In order to calculate the input impedance looking up from that terminal airway, the corresponding tree structure should be used. Let us consider the Horsefield model for the human lung. The tree is constructed based on the following rule: the n_{th} generation, the "**parent**", bifurcates into two daughters; the **left daughter** is always *n-1*, and the **right** one is *n-1-Δ(n)* where *Δ(n)* is the recursion index.

For the sake of simplicity, let us consider the shortest pathway in the human lung model (Fig. 21). The impedance looking up the tree towards the airway opening of the right-most path is equivalent to the input impedance of the network shown in Fig. 22.
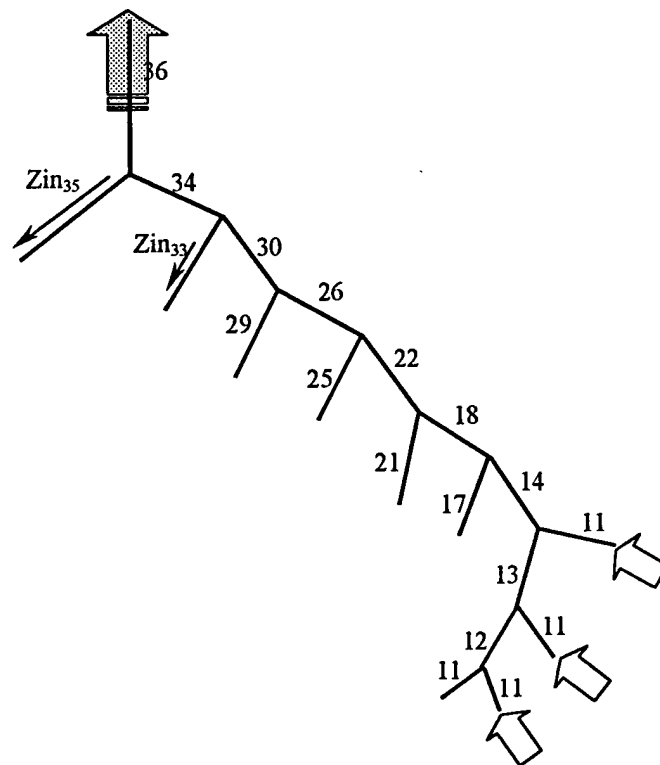
Figure 21. Shortest pathway (down to the order 11) in the Horsefield model of

the human lung

Note that Zin_k is the Zin looking into the k_{th} generation towards the alveoli, all of which have been calculated and stored when computing Zin.
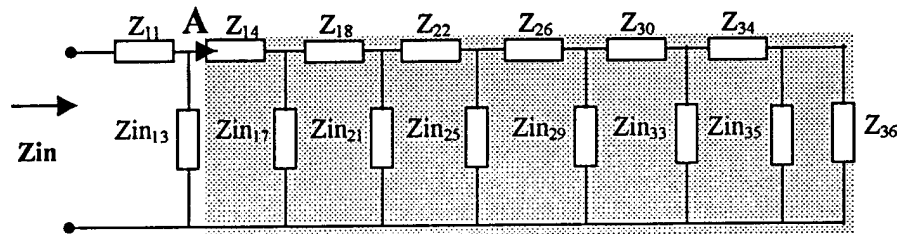
Figure 22 Conceptural network model for shortest pathway in Horsefield's model of the human lung

The input impedance of its adjacent path is equavalent to the the input impedance of the circuit network shown in Fig. 23. Note that the shaded parts in Fig. 22 and Fig. 23 are the same, which indicates that we do not have to re-calculate the impedance along the entire path. In fact, if the impedance looking into A is stored, only the combination of five-elements $\{Z_{11}, Zin_{12}, Z_{13}, Zin_{11}, Zin_A\}$ instead of seventeen-element path needs to be computed in this case.
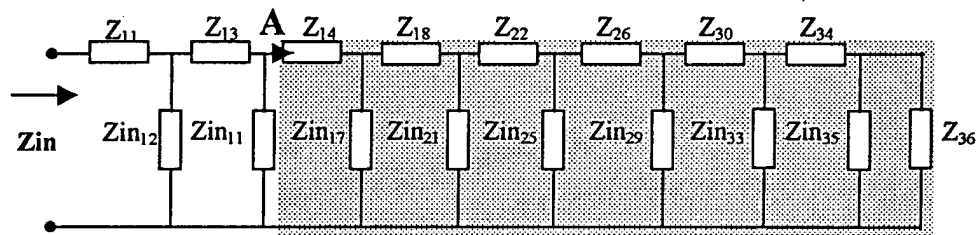
Figure 23. Conceptual network model for the *adjacent* pathway of the shortest in the Horsefield model

3.3.4. Horizontal-decomposition of the tree structure

— symmetrical zone and asymmetrical zone

The Horsefield model describes the branching pattern and dimensions of all the airways in the lung down to and including the respiratory bronchioles. For the sake of computational convenience, it can be decomposed into two structural zones (Fig. 24). In the asymmetrical zone from order 36 to order 12 the branching is asymmetrical, all of which have two different daughter branches (except order 12). The reason to include order 12 in the asymmetrical zone is that order 14 has a recursion index of 2 and has two daughter branches of order 13 and order 11, respectively, such that order 12 is "skipped" in this case.

48
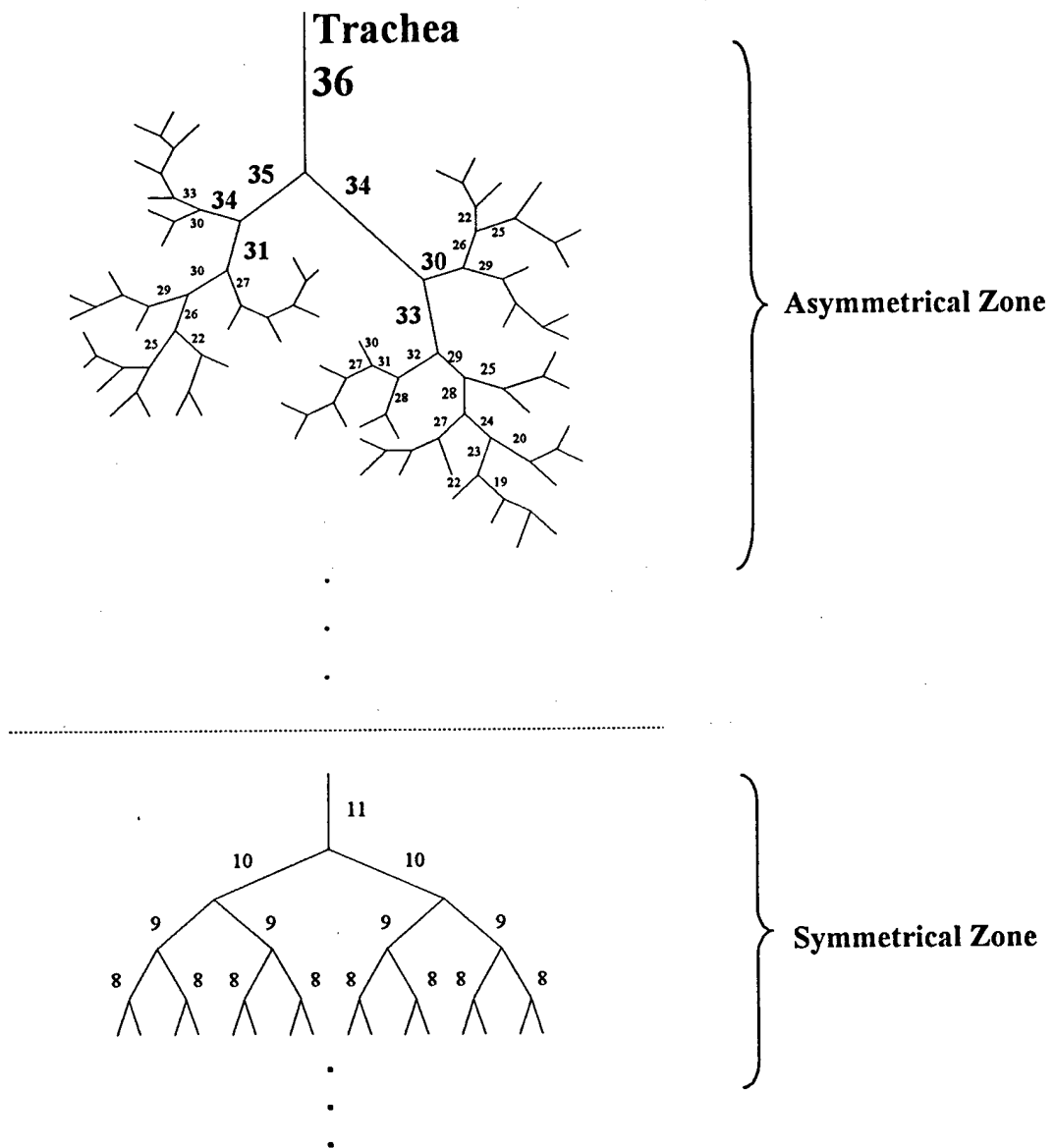
Figure 24. Horizontal decomposition of the asymmetrical tree structure of Horsefield

model

In addition, order 13 has a recursion index of 1, which results in daughter branches of order 12 and 11. The tree structure becomes completely symmetrical from order 11 to order 1. In fact, order 14 to order 12 can be considered as the transition zone. Since there is no computational benefit to having this extra level of decomposition, it is combined with the asymmetrical zone. As one can see, in the symmetrical zone (order 11 to order 1), the structure is symmetrical, which has the computational simplicity and beauty as discussed in section 3.2.

3.3.5. Vertical-Decomposition of the asymmetrical part

In order to solve the problem of limited memory versus large storage needs, further decomposition is required, namely, vertical decomposition (Fig. 25).
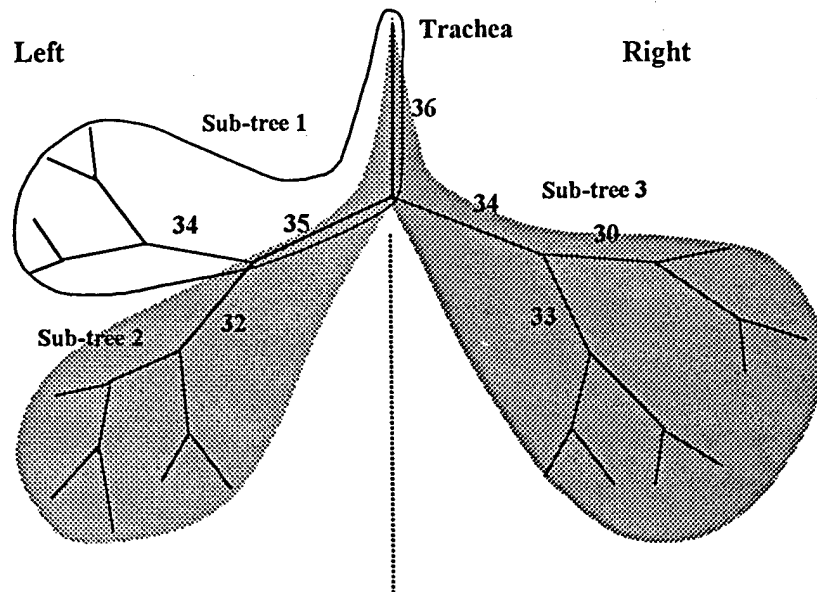
Figure 25. Vertical decomposition of the tree structure

When we compute the input impedances looking from bottom up at most nodes in subtree 1, the detailed structural information of subtree 2 and subtree 3 are not relevant. Therefore, we would rather not use memory to store any parameters related to them. This is more critical when the computational resources are limited while the tree contains a larger number of segments. The three subtrees are almost disjoint in that subtree 1 and subtree 2 only have order 35 and order 36 in common, and subtree 1 and subtree 3 only have order 36 in common. Hence there is little repetition of computation and storage.

3.3.6. Unique indexing binary tree representation of Horsefield model

In the unique-index binary tree (Fig.26), the indices start from 1, which is the index for the root of the tree. If the index for parent branch is n, the indices of the two daughter branches (if they exist) will be:

$$Index\_of\_left\_daughter = 2n \qquad (47)$$

$$Index\_of\_right\_daughter = 2n+1 \qquad (48)$$
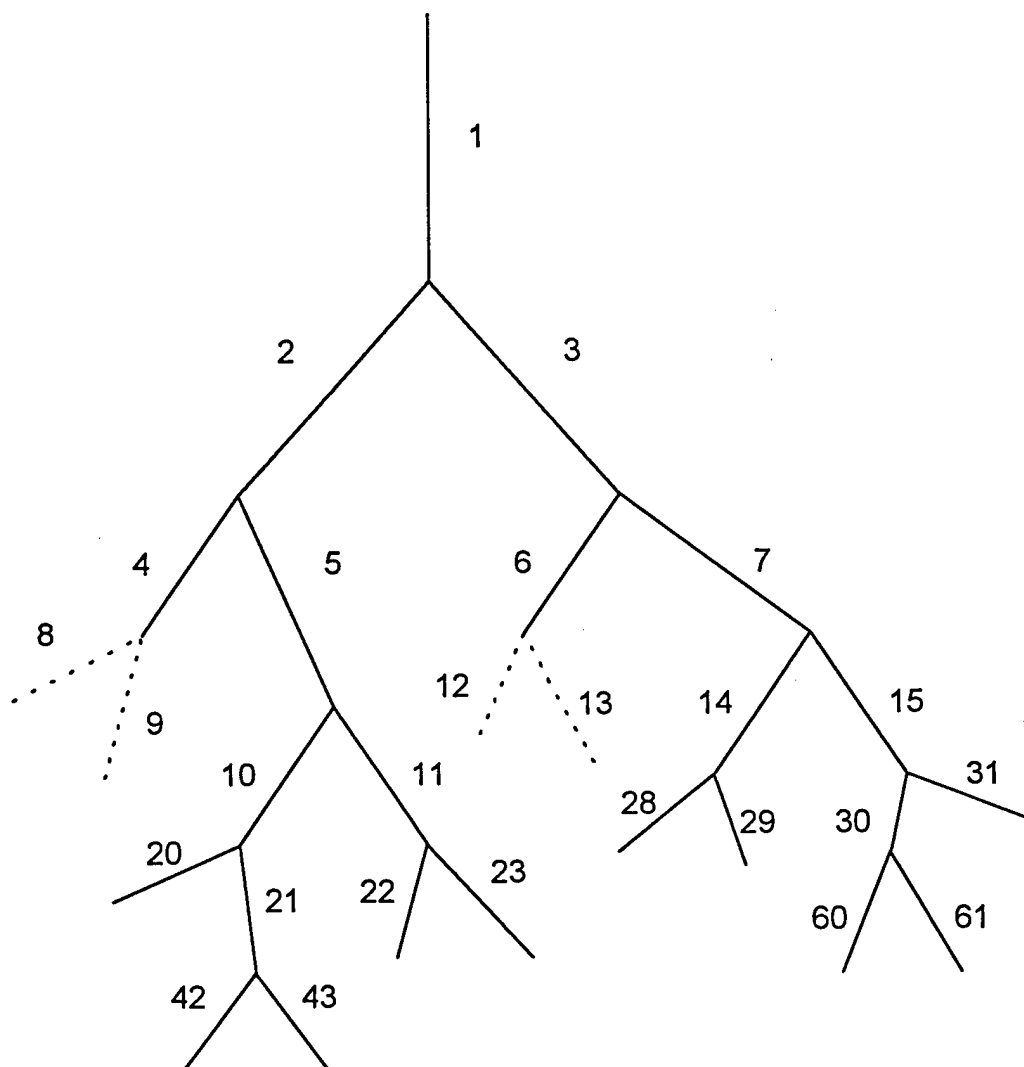
Figure 26. Unique indexing binary tree

One of the advantages of unique-index tree representation is that all airway branches have their own indices such that all of them can be uniquely identified and computed individually. Another more important advantage is that the numbering itself "indicates" the position of the branch in the entire network in that its parent, grandparent, up to the root of the tree can be derived from its index. The parity of the index indicates whether it is on the left or on the right, and therefore its neighbor can be identified as well. This is illustrated in Fig. 27. For a given branch whose index is 13, let us find the path to get here:

1) *Since 13 is odd, this branch must be a right daughter branch, and its neighbor (on the left) is 12. The index of its parent is* $\left\lfloor \dfrac{13}{2} \right\rfloor$ *(*$\lfloor x \rfloor$*: "floor of x", the greatest integer $\leq$ x), which is 6.*

2) *6 is even, so it is on the left and its right neighbor is 7. Its parent is* $\left\lfloor \dfrac{6}{2} \right\rfloor = 3.$

3) *3 is odd, so it is on the right and its left neighbor is 2. Its parent is 1, which is the root of the tree.*

Note that if the index i of the branch is odd, its neighbor's index is $i - 1$. Otherwise its neighbor's index is $i + 1$;

53
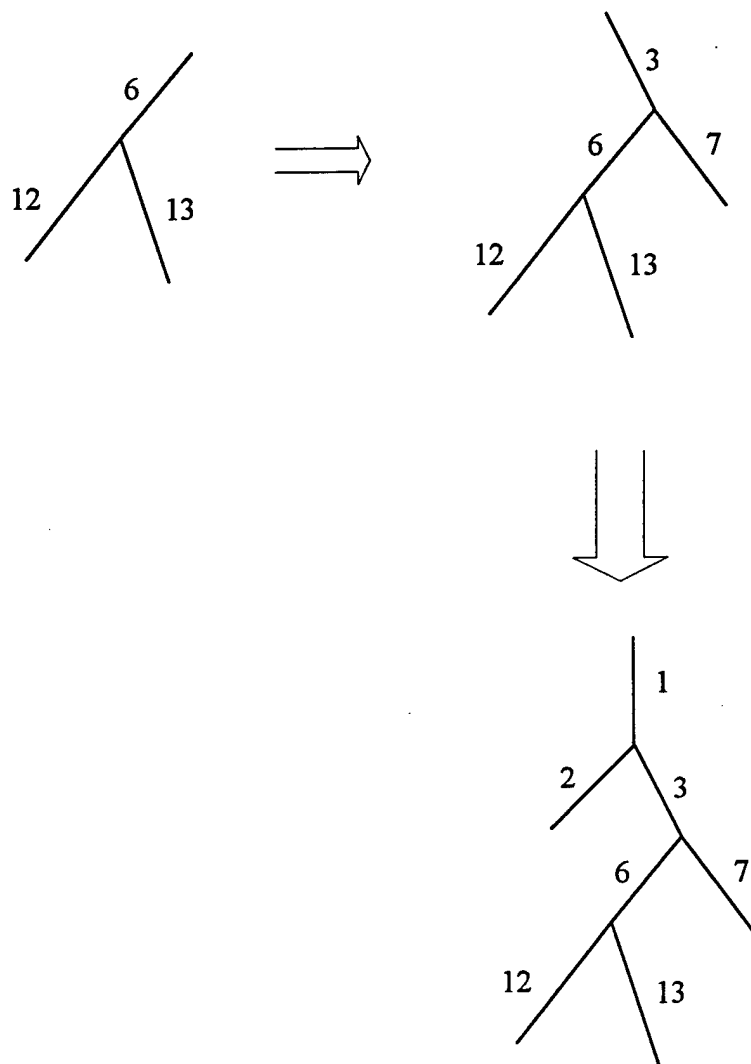
Figure 27. Illustration of retrieving the entire path from the root of the tree to a given branch.

This turns out to be a powerful feature when implementing the algorithm for computing the transfer impedance Z_{tr} since searching is straightforward.

However, the actual morphometric data are associated with Horsefield order number. Therefore, it is necessary to map the Horsefield's model onto unique-indexing binary tree representation. For a given unique index, the corresponding Horsefield order number will indicate where to find the morphometric data. The two indices are mapped in Table 9:

Table 9. Mapping Horsefield model to Unique index representation

	Unique index representation	Horsefield model
Root of the tree	1	N (total number of orders)
For a given branch	n	k
Left daughter	2n	k-1
Right daughter	2n+1	k-1-Δ(k)

3.3.7. Recursive algorithm for searching all the airway paths

For a given destination, i.e. K_{th} order, the following algorithm is used to obtain all the possible pathways when starting from the n_{th} order.

For left branch (node):

```
Function lnod((n, k, path, flag)

if(n>K)         % if haven't reached the destination yet

    n=n-1;      %  keep going down left further

    if(n==K)    % if reached the destination, record
```

55

```
        print [path, n]

        print [flag, 0]

    elseif(n>K)  % keep going

      lnod(n,K,[path,n],[flag,0]);

      rnod(n,K,[path,n],[flag,0]);

    end;

  end;
```

For right branch (node):

```
Function rnod(n, k, path, flag)

if(n>k)          % if haven't reached the destination yet

  n=n-1-delta(n);  %  keep going down right further

  if(n==k)

      print [path, n]

      print [flag, 1]

    elseif(n>k)

      lnod(n,k,[path,n],[flag,1]);

      rnod(n,k,[path,n],[flag,1]);

    end;

  end;
```

The algorithm is fairly simple. The speed of the algorithm depends on the maximum

pathway length (how many to go through) and the recursion indices.

3.3.8. Transfer impedance

In the asymmetrical zone of the Horsefield's model, all of the paths end with order 12, 13 or 14 (Fig. 28). The number of paths and the number of nodes, which is equal to the number of different input impedances, of sub-tree 1 are listed in Table 10. Starting from the top of each path we compute the input impedances looking from bottom up. If the input impedance of the node (the end of the corresponding airway branch) has already been calculated, we skip it and look at the next one on the path until the end is reached.
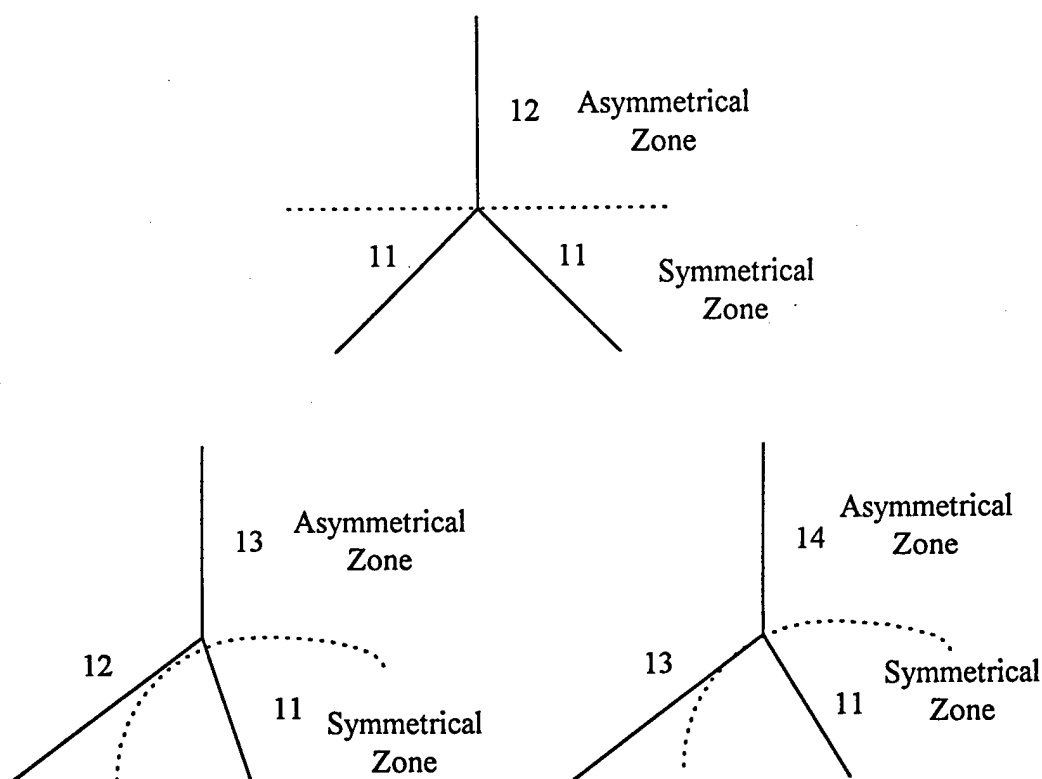
Figure 28. Illustration of the three possible ways which all the paths in three subtrees can end with.

57

Table 10. The number of paths and nodes in Sub-tree 1

Path ends at:	Order 12	Order 13	Order 14
Number of paths	907	476	345
Total number of paths	1728		
Total number of nodes	2633		

As one can see that all these paths have many nodes in common. We avoid repeating the computation of the input impedance of the same node by determining whether the unique index of this node has been marked.

For the symmetrical zone (from order 11 to the most peripheral terminal airways), the methods discussed in section 3.2 are applied to obtain the equivalent two-port network block T_{sym} combining airways from order 11 to 1 and the tissue properties (Fig. 29). The impedance looking up from the last node of a given path, in parallel with the input impedance of the neighbor of order 11th, serves as the load impedance of this two-port network.
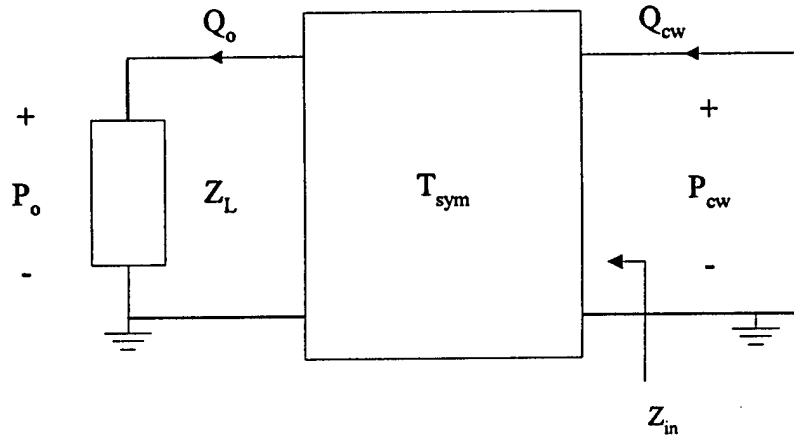
Figure 29. Two-port network representation of symmetrical zone

The output pressure of the two-port network, T_{sym}, is the equivalent pressure source to the corresponding path in asymmetrical zone. Here, m in Eq. (22) is 2^{11-n}, where n is the order number in Horsefield's model. N_{ends} in Eq. (30) is 2^{10}, instead of total number of terminal airways.

Therefore, proceeding up the path in the asymmetrical zone, the pressure at the end of trachea and the flow at the airway opening can be computed. The sum of all flows due to all of the identical applied pressure sources is the total flow in the trachea, $\Sigma Flow_k$. Dividing the pressure by this flow sum gives the transfer impedance,

$$Z_{tr} = \frac{P}{\Sigma Flow_k} \tag{49}$$

3.3.9. Pressure ratio distribution along the shortest path

To compute the distribution of pressure ratios along the shortest path in the asymmetrical zone, a tractable organization of the entire tree network is needed. The entire tree is re-organized (pruned) with respect to the shortest path (Fig 30) into seven subtrees. The equivalent flow sources from the corresponding sub-trees are identified as flow_1 through flow_7. The nodes where the pressure ratios are computed are labeled accordingly (1 through 7). The flow from a given source (i.e., flow_n) at each (k^{th}) of seven nodes will be downward if $n < k$ and upward if $n \geq k$. The flow due to all the flow sources is then computed using the superposition theorem. Since the impedance at each node is known, the pressure at that node can be computed in a straightforward way and normalized to the applied pressure.
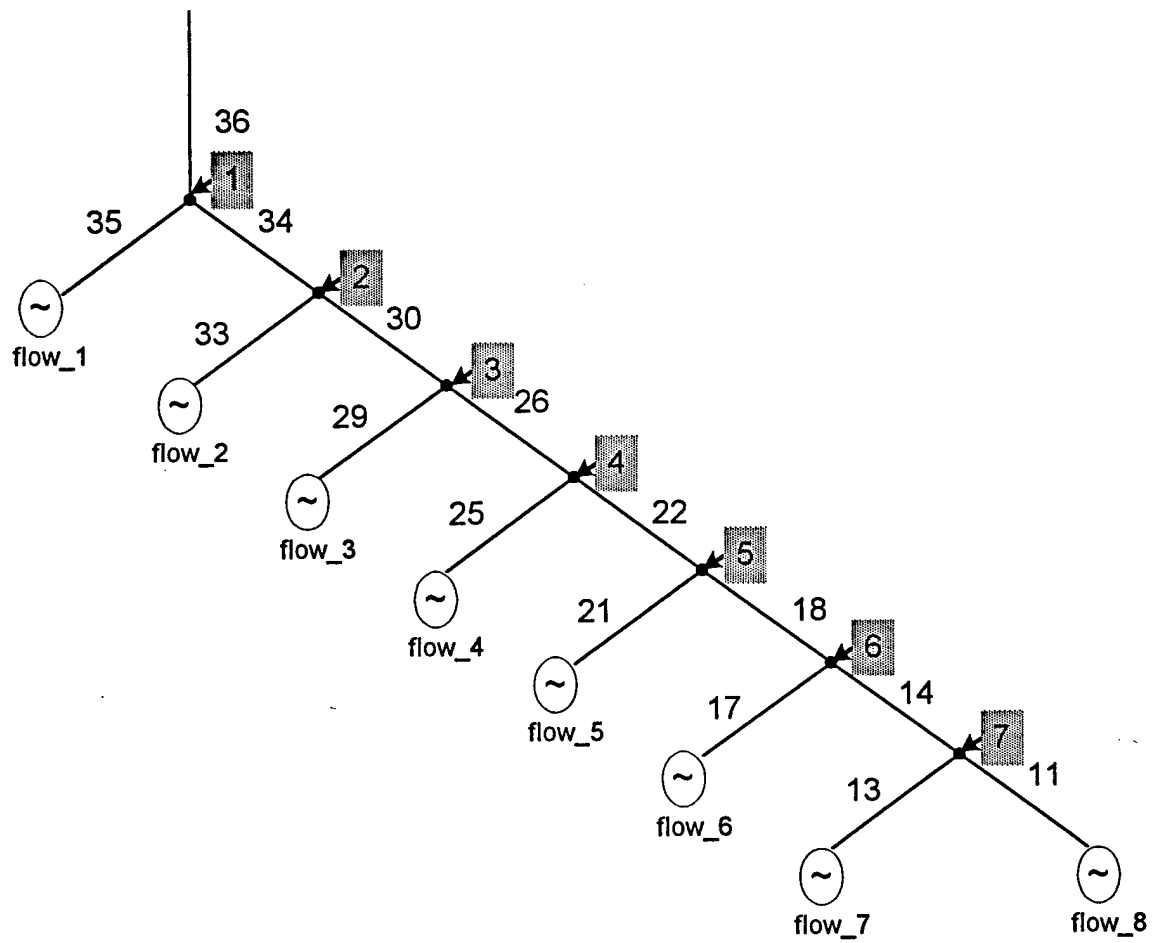
Figure 30. Equivalent flow sources along the shortest path

4. Results and Discussion

4.1 Symmetrical model versus asymmetrical model

4.1.1 Input impedance Z_{in} of the human lung models

Weibel's symmetrical model (Table 1) and Horsefield's asymmetrical model (Table3) both combined with non-rigid airway wall parameters (Table 5 and Table 4, respectively) were used to simulate Zin (Fig. 31). Note that neither model included the upper airways. The first anti-resonance in Weibel's symmetrical airway network occurs at a lower frequency than it does in Horsefield's asymmetrical airway network. The dominant factor that accounts for the differences in the frequency of this anti-resonance is the length difference in the trachea rather than the symmetry of the airway network. In Weibel's model, the trachea is 12 cm in length while it is 10 cm long in Horsefield's model. This complies with the fact that the frequency of the acoustic resonances and anti-resonances in a tube is inversely related to its length. The experimental Zin data published by Habib et al. [1] are shown in Fig. 31 (b) for comparison to the model predicted Z_{in}. The Z_{in} predictions from both symmetrical and asymmetrical airway network compare closely to the measured data.
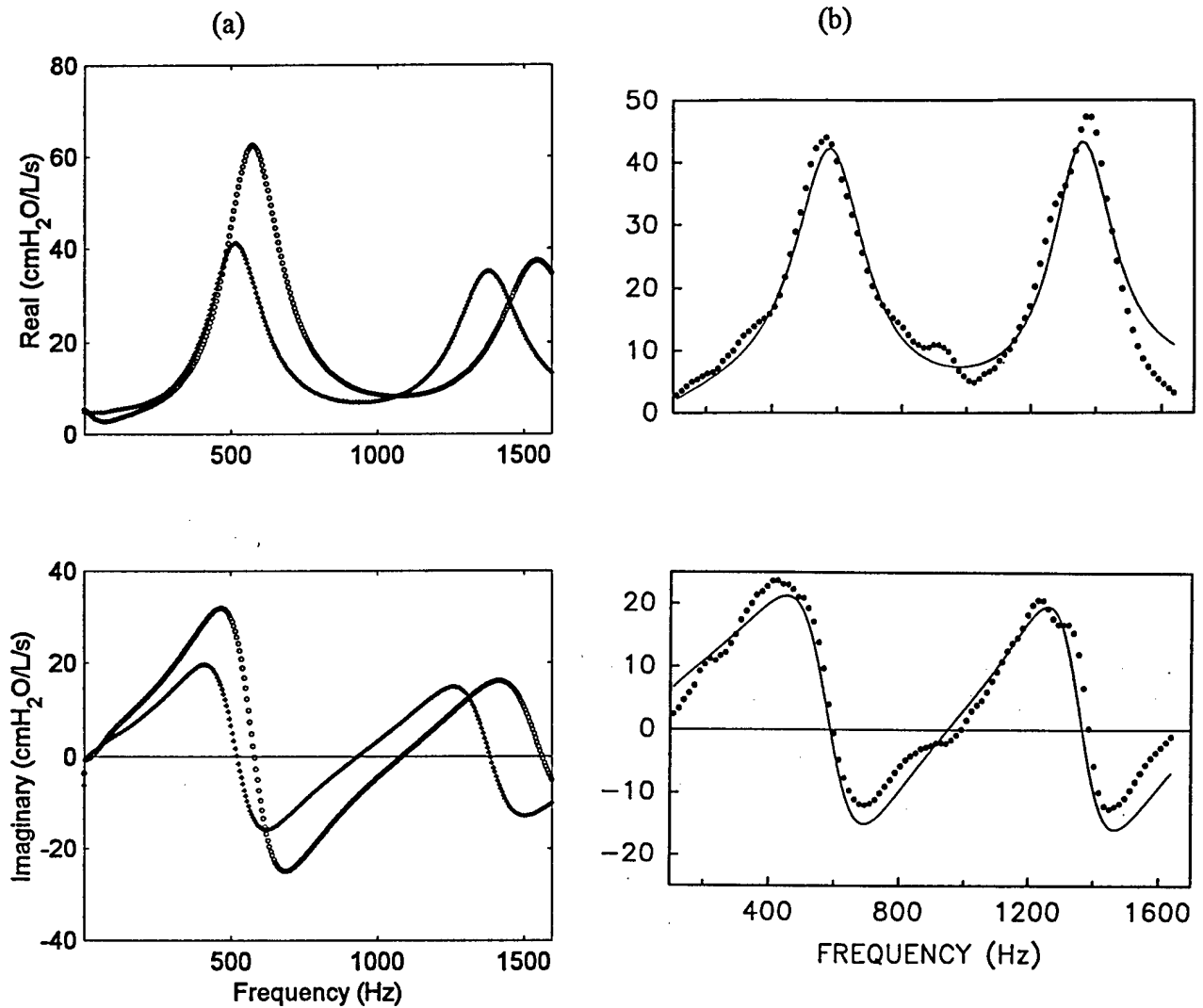
Figure 31. (a) Z_{in} based on Weibel's symmetrical airway network (*) and Z_{in} based on

Horsefield's asymmetrical airway network (o)

(b) Subglottal (i.e., without upper airways) Z_{in} data (•) measured in adult

human (Habib et al. [1])

4.1.2 Total respiratory input impedance including upper airways

The total respiratory Zin including upper airways was simulated and compared to measured data [22] (Fig. 32). The resonant peak is shifted to lower frequencies compared to subglottal Zin due to the added airway length. Summing the lengths of the upper airways from Table 7, we have a total length of 23.2 cm for the upper airways.

Real (*top*) and imaginary (*bottom*) parts of human input impedance averaged from all 8 subjects (Table 1). Mean (*) ± SD (———). Units of impedance are $cmH_2O \cdot l^{-1} \cdot s^{-1}$.
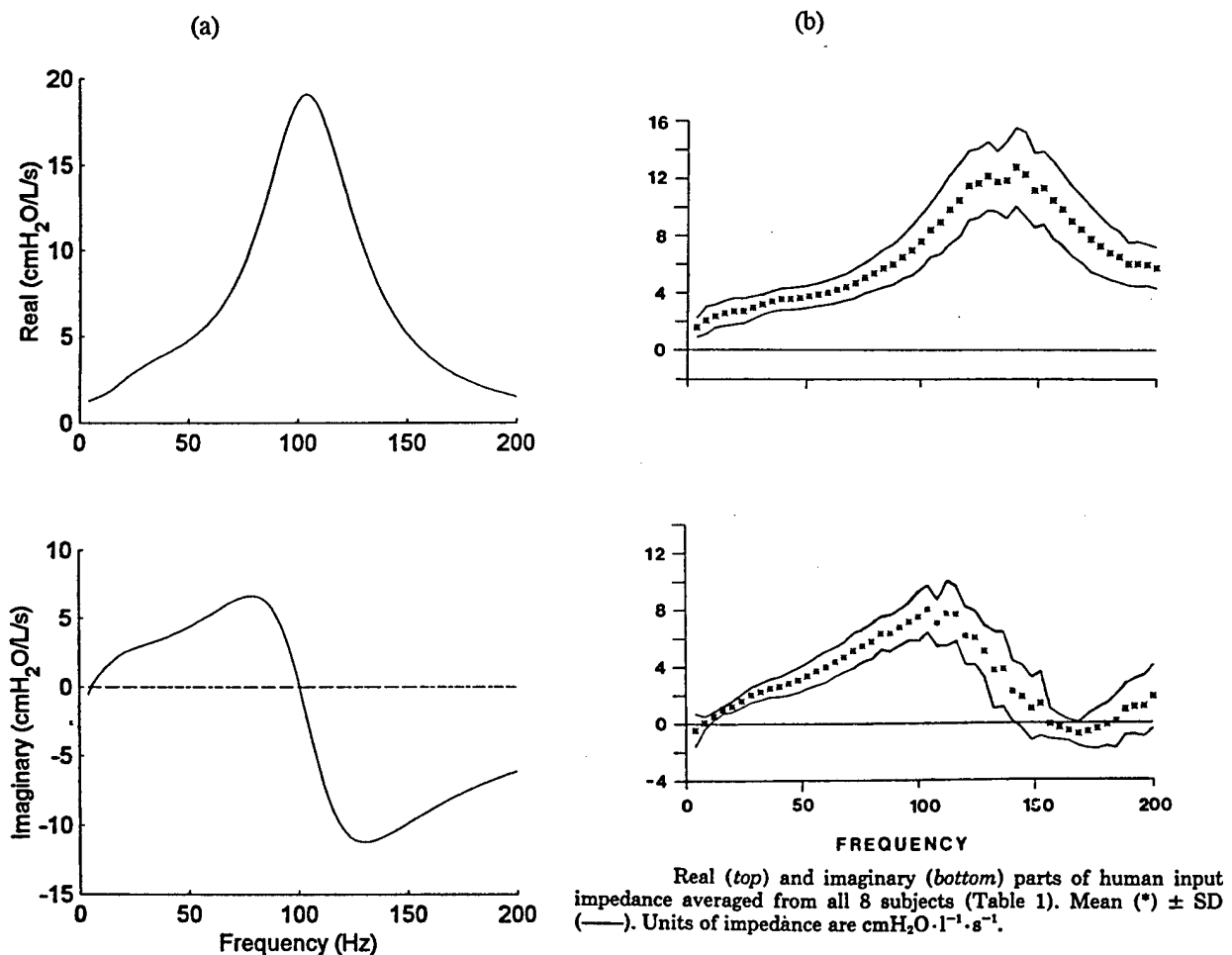
Figure 32. (a) Total respiratory Z_{in}. (b) Z_{in} data measured in adult human (Dorkin, H. L. et al. [22])

4.1.3 Z_{tr} from Weibel's model versus that from Horsefield's model.

Z_{tr} is usually measured with the setup shown in Fig. 2 (a). The forced oscillation is placed around the chest wall, and flow is measured at the airway opening. Since the mouth of a subject is open, the impedance to flow at the airway opening is extremely small and modeled as a short circuit (Fig. 18). The upper airways influence the measurement, and therefore, they were included in the simulations. Z_{tr} was computed from 1 up to 72 Hz in both the symmetrical and asymmetrical models and compared with measured data published by Lutchen et al [7] (Fig. 33).

To explore Ztr at higher frequencies in more detail, we simulated it up to 1000 Hz using the symmetrical and asymmetrical models (Fig. 34). They are very similar except in the symmetrical airway model the anti-resonance occurs at a lower frequency than in the asymmetrical airway model. Again, this is most likely because of the longer trachea in the symmetrical model.
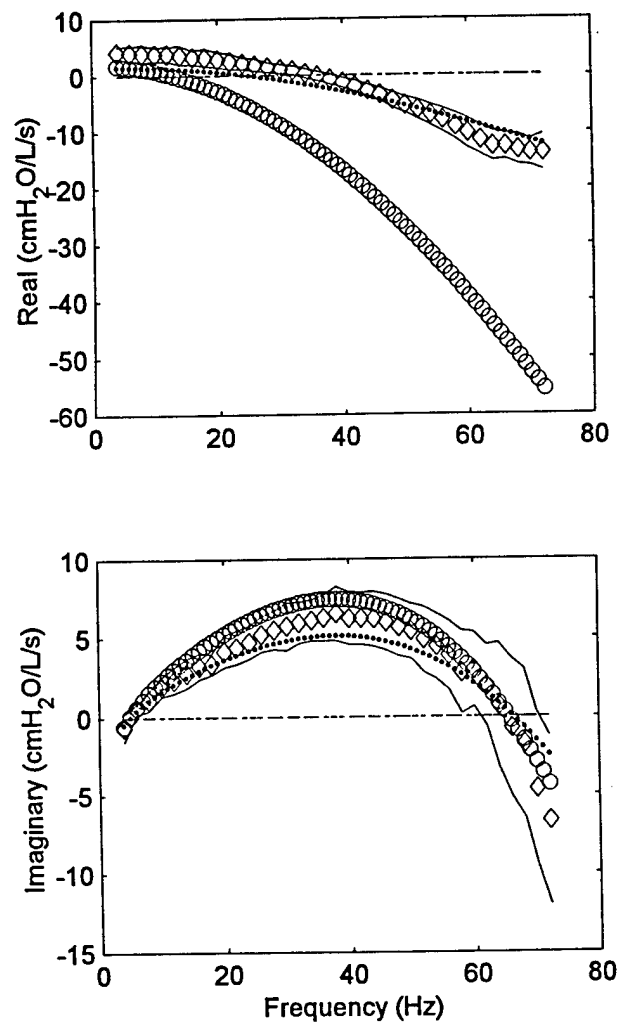
Figure 33. Ztr of the symmetrical human lung model (•), Ztr of the asymmetrical human lung model (o), and measured data (average '♦' ± SD '-') at low frequencies..
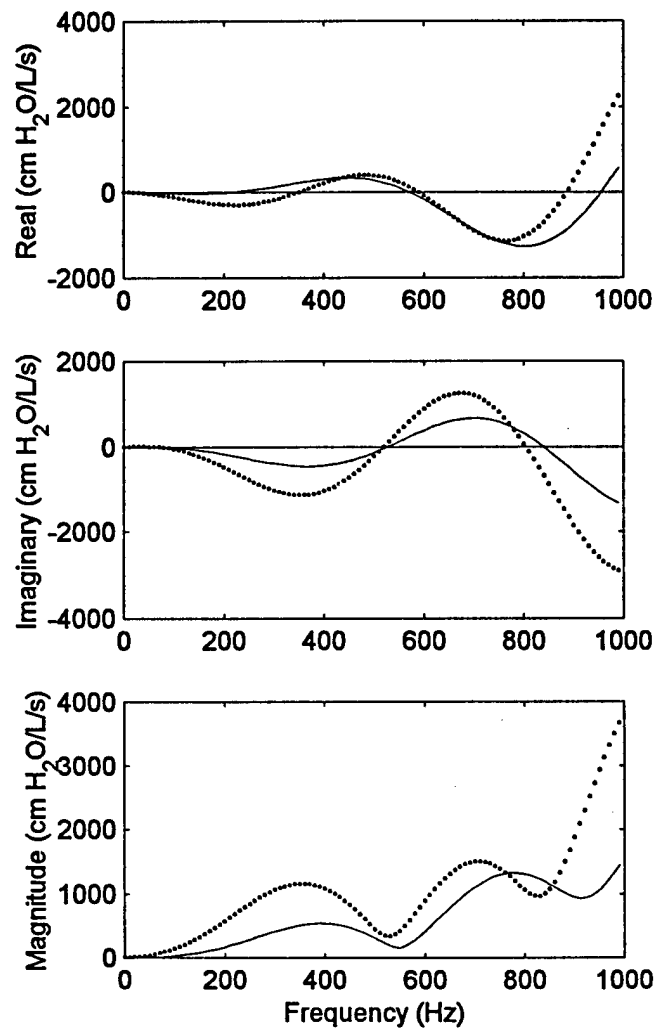
Figure 34 Ztr of the Weibel's symmetrical human lung model (•) and Ztr of the Horsefield's asymmetrical human lung model (-) at high frequencies

## 4.1.4 Pressure ratio distribution with forced oscillation imposed at the airway opening

It has been reported that in Horsefield's dog lung model the serial pressure distributions are frequency-dependent and pressures in the peripheral airways and alveoli at some frequencies can be larger than at the airway opening [20]. We were interested to know whether this was also the case in the asymmetrical human lung model. First, we simulated the pressure ratio at low frequencies from 1 to 100 Hz along the longest pathway in the human lung model (Fig. 35 (a)). We found that the ratio of alveolar pressure, P_{alv}, to airway opening pressure, P_{ao}, is greater than unity below 5 Hz, which agrees with the findings of Jackson et al in the dog lung [20]. The maximum of the pressure ratio is about 1.27 and occurs at 4 Hz. Pressures were amplified below 5 Hz in all the airway orders from the most peripheral airway to the upper airways. The maxima of the pressure ratios in all airway orders occur at 4 Hz (Fig 35 a), and at this frequency the pressure ratio reaches its maximum in airway order 15 (Fig 35 b). To compare our predictions in the human model to those of Jackson et al (20), we predicted the pressure ratios in the trachea and alveoli (Fig 35 c, d).
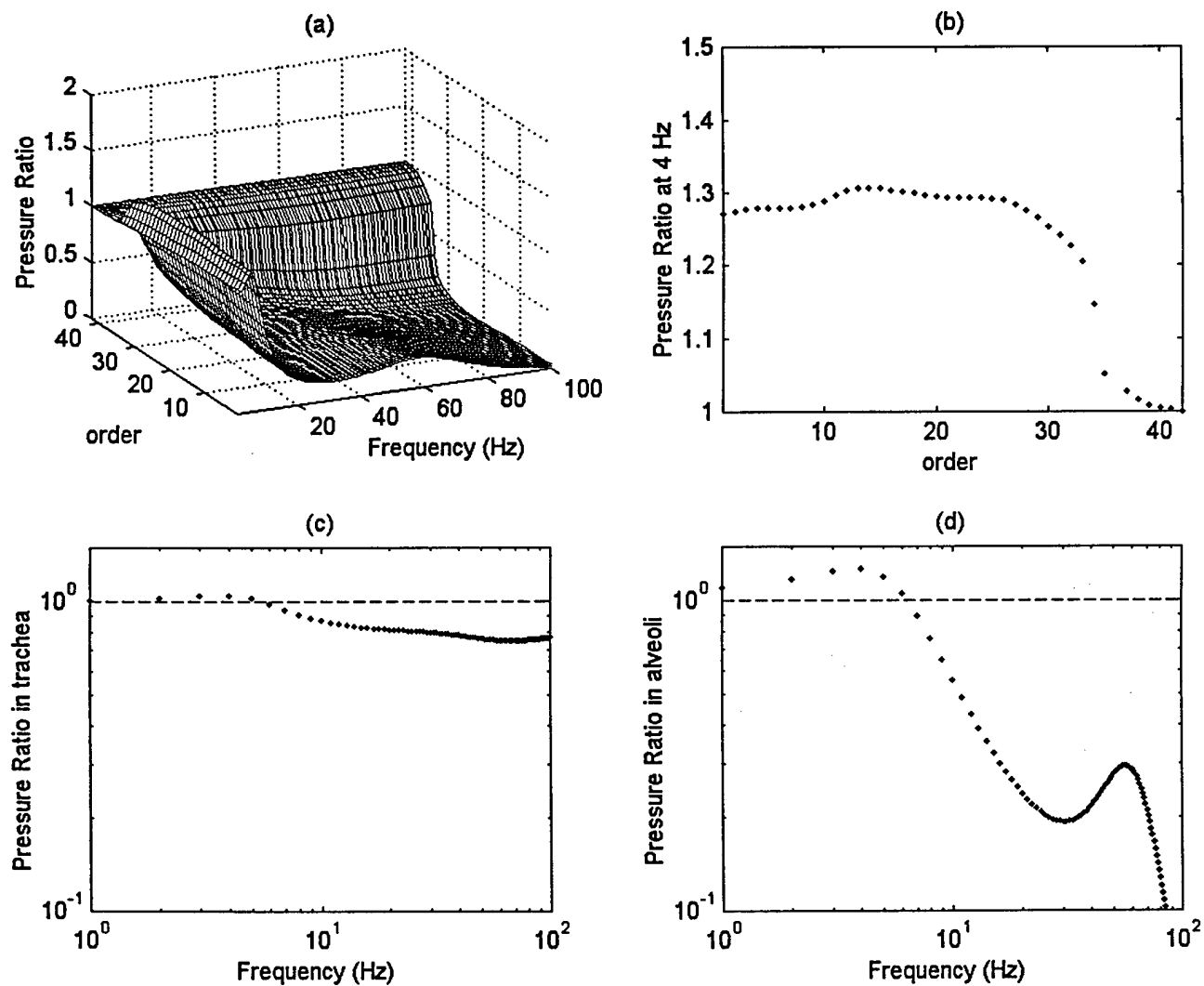
Figure 35. Pressure ratio distribution at low frequencies. (a) Pressure ratio distribution versus frequency and airway order. (b) Pressure ratio versus airway order at 4 Hz, where the maximum occurs. (c) Pressure ratio in the trachea (36th order). (d) Pressure ratio in the alveoli (1st order)

We further explored the distribution of the pressure ratios at frequencies up to 2200 Hz (Fig. 36 (a)) and found that pressures in the central airways can be 6 to 10 times higher than P_{ao} at certain frequencies, i.e., approximately 400 Hz, 800 Hz, and 1600Hz. Fig. 36 (b), (c) and (d) illustrate in detail the pressure ratios in the upper airway (41st order), the trachea (36th order) and the peripheral airway (1st order), correspondingly. Quite different from what was found at low frequencies, the pressure ratios are much higher in the central airways than in the peripheral airways. There is no pressure amplification in the peripheral airways for $f > 5$ Hz.
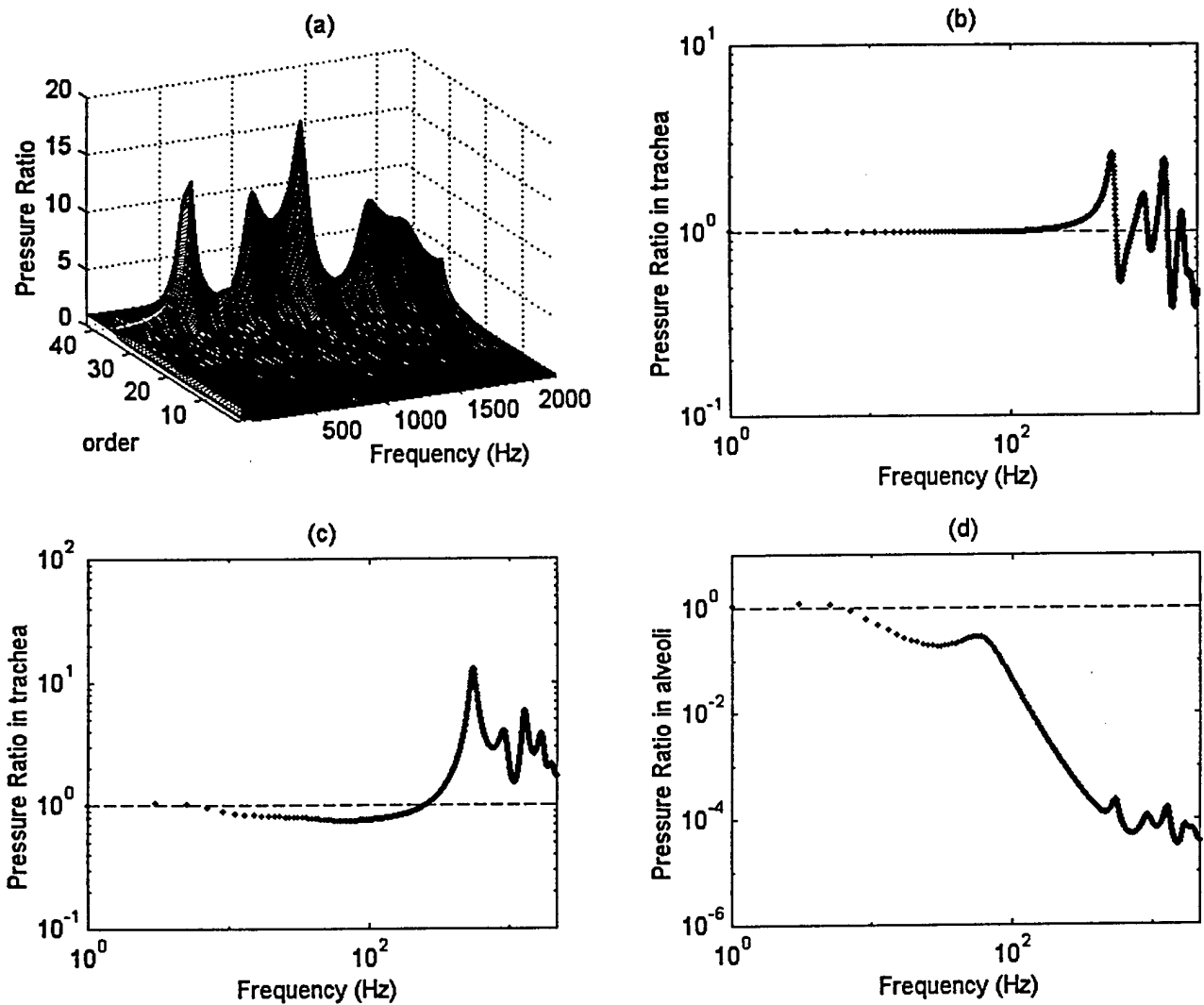
Figure 36. Pressure ratio distribution at high frequencies. (a) Pressure ratio distribution versus frequency and airway order. (b) Pressure ratio in the upper airway (41st order). (c) in the trachea (36th order). (d) in alveoli (1st order)

4.1.5 Pressure ratio distribution with forced oscillation imposed at the chest wall

To investigate the potential influence of low frequency sound (LFS) on divers, we simulated the pressure ratios versus frequency and airway order. The pressure distribution was simulated for a boundary condition where $Z=\infty$ at the airway opening, i.e., closed mouth and closed nasal passage. This is analogous to having an open circuit at the airway opening. The pressure ratios as a function of frequency (up to 250 Hz) and airway order were first simulated using the symmetrical model and no pressure amplification was found (Fig. 37 (d)). In fact, in all airways the pressure decreases significantly as frequency increases. The maximum pressure ratio occurs at the lowest frequency (used 1 Hz) and the pressure ratio is relatively independent of airway generation. Intuitively, it is difficult to understand why there would be such a small pressure change along the airways. Since pressure is related to impedance and flow, it is natural to study impedance and flow distribution versus airway generation. In the equivalent series two-port network (Fig. 19), the impedance (Z_{cw-ao}) looking from the chest wall up the airway tree as a function of airway order at 1 Hz is shown in Fig. 37 (a). The flow (Fig. 37 b) as a function of airway order decreases from the alveoli to the airway opening while Z_{cw-ao} increases. This is a reciprocal process resulting in little change in the pressure ratio (Fig. 37 c).
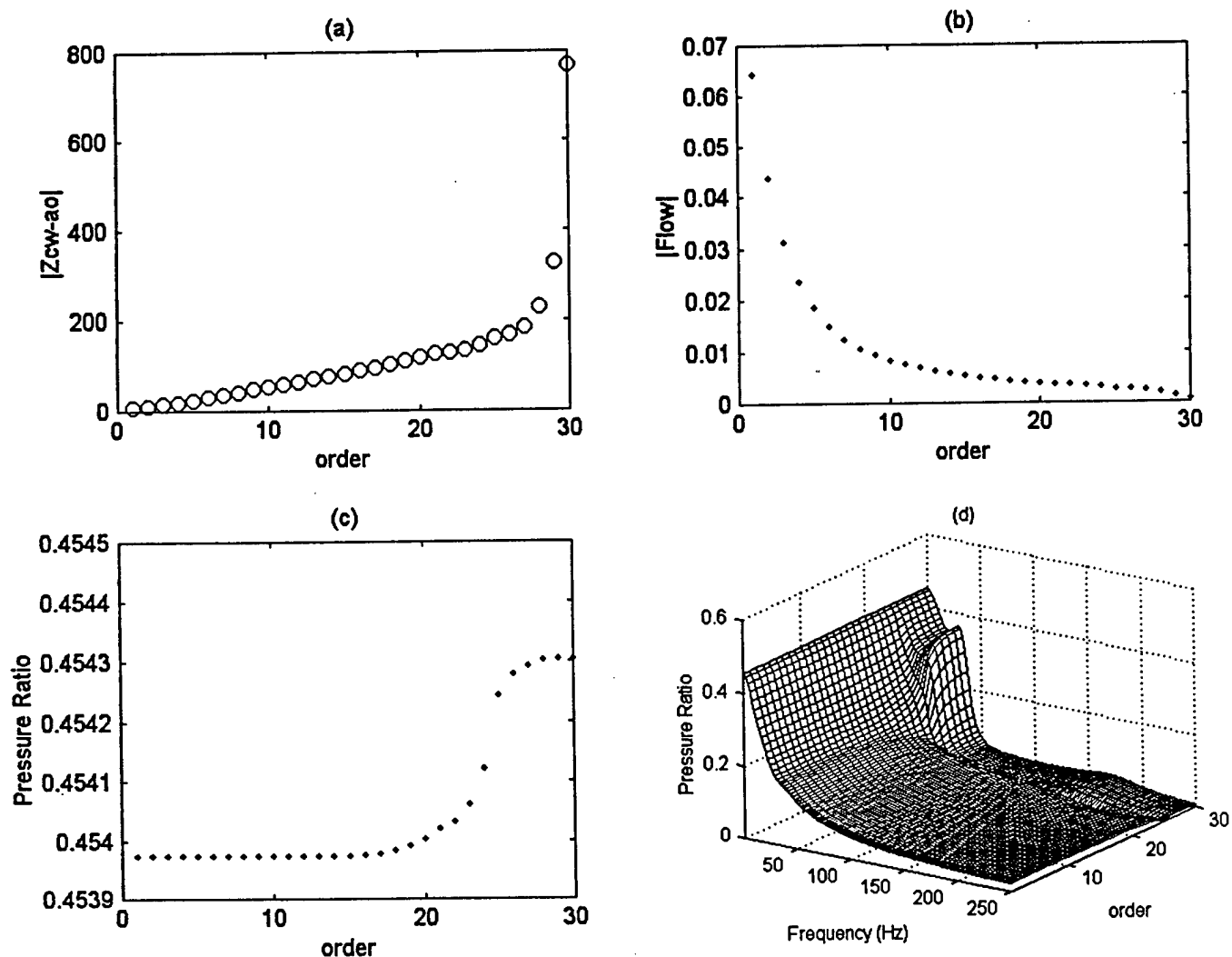
Figure 37. Pressure ratio distribution in the Weibel's symmetrical airway network.

(a), (b) and (c) Z_{cw-ao}, flow, and pressure versus airway order at 1 Hz.

(d) pressure ratio distribution as a function of frequency and airway order.

The pressure distribution in the asymmetrical airway model depends not only on the airway order, but also on the path taken to a particular airway segment. Simulating the pressure ratio distribution over the entire airway network using the superposition model is not a trivial task. Thus for simplicity, we took the shortest pathway as the representative pathway and simulated the pressure ratios along this path. To further simplify the simulation, the airways below the 14th order were not included since these airways branch symmetrically and nothing interesting was found in peripheral airways in the symmetrical airway network (Fig. 38 (d)). The pressure ratio is greater than unity (i.e., pressure amplification) at ~40Hz in the trachea and upper airways (Fig. 38 (d)). We found a significant drop in the pressure ratio going from the trachea into the next airway order. To study this further, we plotted the input impedances looking from the chest wall towards the airway opening (Z_{cw_ao}) and flow as a function of airway order. A large impedance drop was found between the trachea (36th order) and the 34th order airway. The difference between the symmetrical and asymmetrical models is that the magnitudes of both Z_{cw-ao} and flow are increasing when proceeding from the peripheral airways to the upper airways. This may explain why the pressure ratio distribution in the asymmetrical model looks very different from that of the symmetrical model.
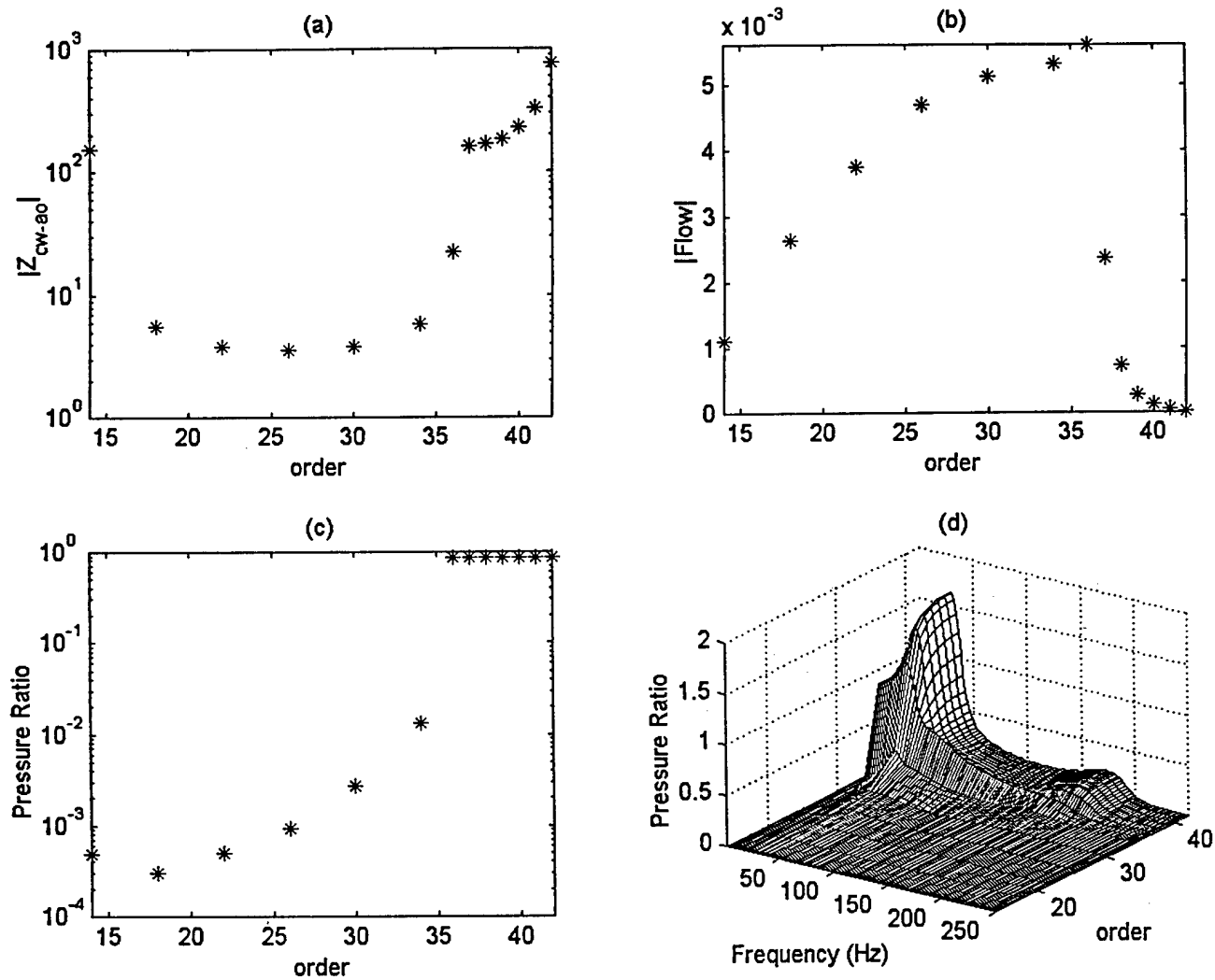
Figure 38. Pressure ratio distribution in the Horsefield's asymmetrical airway network.

(a), (b) and (c) Z_{cw-ao}, flow, and pressure versus airway order at 1 Hz.

(d) pressure ratio distribution as a function of frequency and airway order.

4.2 Strain, wave propagation velocity and wall admittance distributions in asymmetrical airway network

4.2.1 Strain as a function of frequency and airway order

It is not clear whether barotrama in the airways is due to excessive pressure (stress) or deformation (strain) of the airway wall (i.e., the motion or displacement of the airway wall). For example consider two different airways that are exposed to a transmural pressure oscillation of the same magnitude; if one has a smaller magnitude of impedance it would experience a larger strain. Strain in a tissue is usually defined as

$$\epsilon = (L - L_0)/L_0 \tag{50}$$

where L_0 is the tissue's resting length and L is its deformed length. However, here we will consider the volume strain of an airway segment where volume strain, ϵ_v is defined as

$$\epsilon_v = (V - V_0)/V_0 \tag{51}$$

where V_0 is the resting volume of the airway segment and V is its maximally deformed volume. The magnitude of the time derivative of an airway segments ϵ_v is the magnitude of its volume flow and is related to its wall impedance and the transmural pressure by,

$$d\epsilon_v/dt = P_{tm}/Z_{aw}. \tag{52}$$

The pressure and thus the flow will be a sine function, or

$$d\epsilon_v/dt = A\sin(\omega t). \tag{53}$$

The magnitude of the segment's volume change ΔV, is

$$\Delta V = \int flow\ dt = \int A\cdot\sin(\omega t)dt = A\cdot\cos(\omega t) / \omega \tag{54}$$

Thus the amplitude of ϵ_v is given by

$$\epsilon_v = A / \omega \tag{55}$$

The values of ϵ_v within the airway tree depend on the amplitude of the applied pressure (i.e., Pao when applied at the airway opening, or P_{bs} when applied at the body surface). Thus, we predicted ϵ_v for a unity P_{ao} and P_{bs} (Fig. 40). The strain is normalized to its maximum value and therefore the maximum strain is unity. The volume strain ϵ_v is a maximum at approximately 30 Hz and occurs in the central airways.
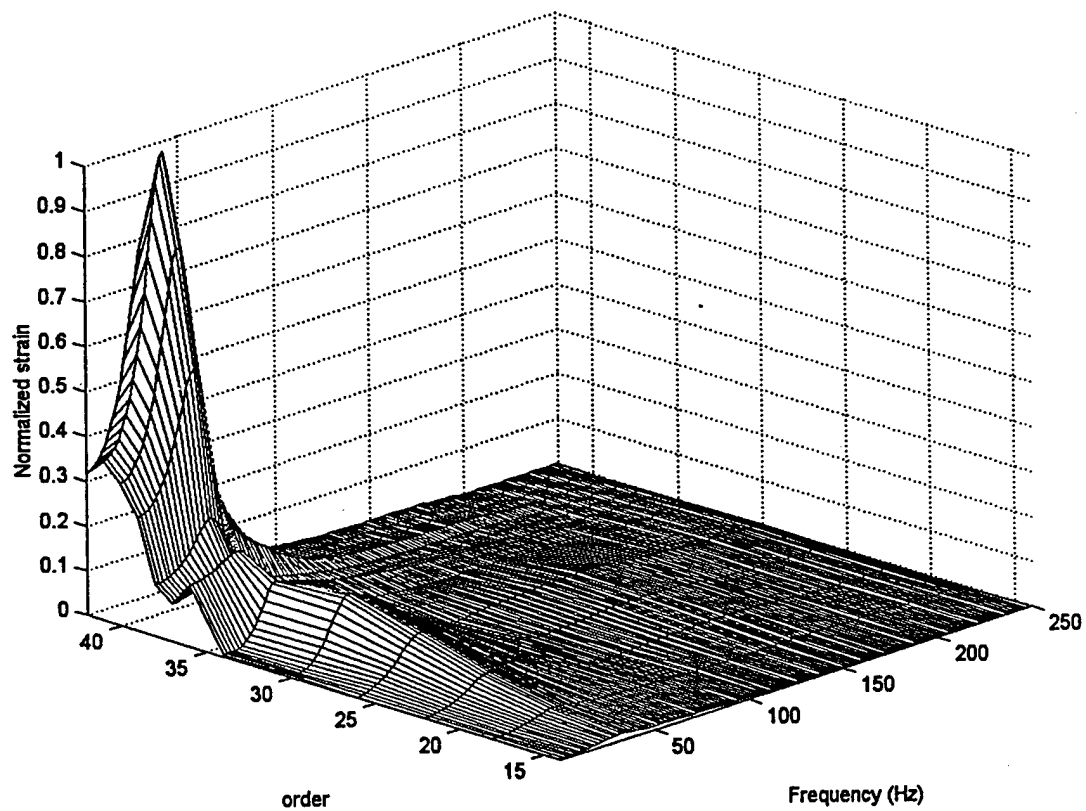
Figure 40. Strain distribution versus frequency and airway order

4.2.2 Wave propagation velocity as a function of frequency and airway order

In rigid-walled tubes, the velocity of wave propagation is equal to the free-field speed of sound (34,318 cm/s in room air). However, in nonrigid-walled tubes, wave propagation velocity becomes frequency dependent [21]. The wave propagation velocity distribution as a function of frequency and airway order are shown in Fig. 41.
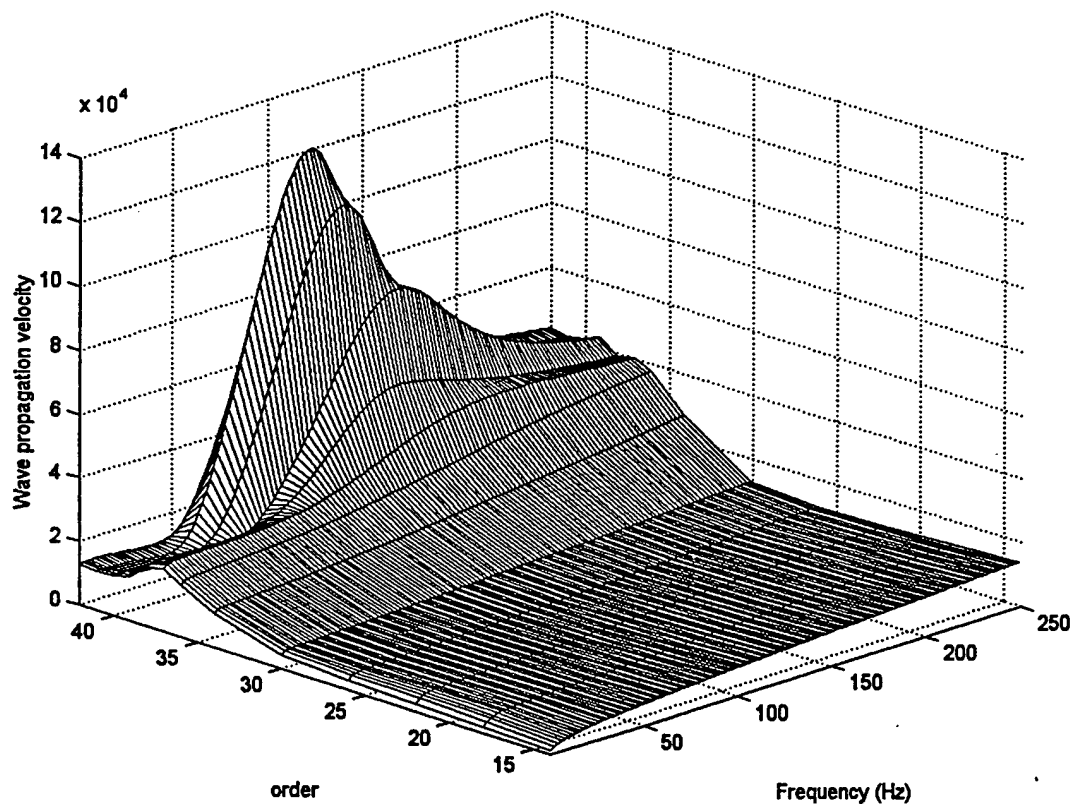
Figure 41. Wave propagation velocity distribution as a function of frequency and airway order.

4.2.3 Relationship between strain and wave propagation velocity

If the shunt admittances of a nonrigid walled tube are significantly under-damped (i.e., their resistance is small), sound may not be propagated at or near its resonant frequency because wave propagation velocity could become less than zero (Fig. 42). At frequencies where c<0, there would be extremely large volume strains and no energy would be propagated since it is all dissipated in wall motion.
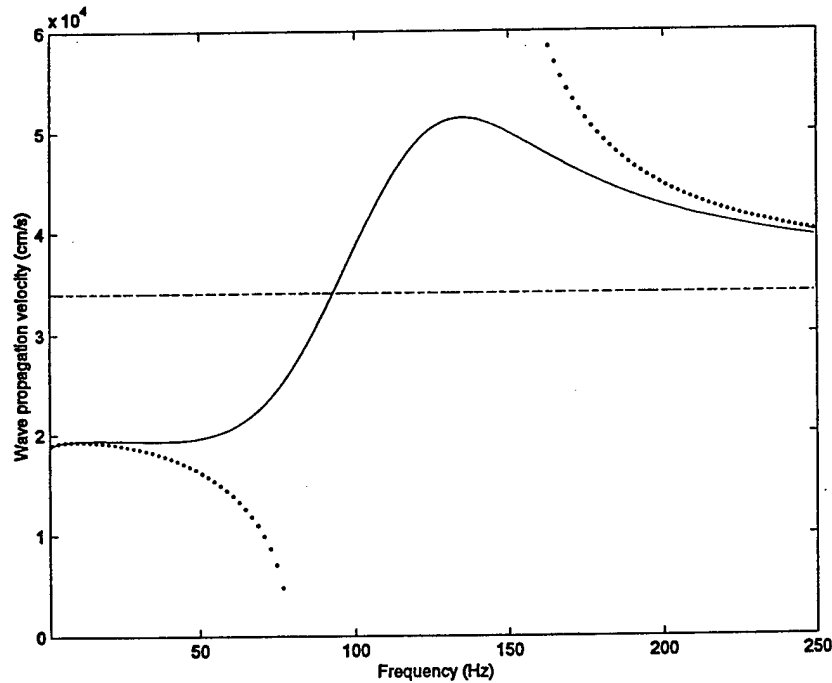
Figure 42. Wave propagation velocity with no propagation at certain frequencies

To explore the relationship between strain and wave propagation velocity, we plotted them together in Fig. 43. These are the projections on the frequency axis of their 3-D plots, shown in Fig. 40 and Fig. 41, respectively. Different curves represent different airway orders. As we expected, the regions of maximum stain correspond to the regions of minimum wave propagation velocity, as indicated by dashed line boundaries.
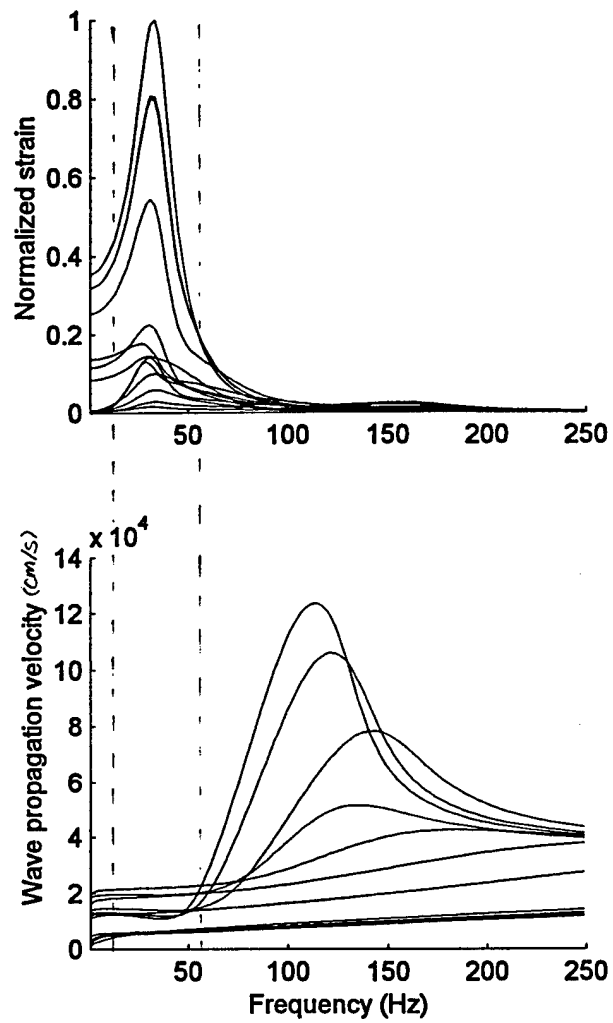
Figure 43. The relationship between the strain and wave propagation velocity.

4.2.4 Relationship between strain and airway wall admittance

We took the airway segment (order 41st) in which strain achieves its maximum, as the representative to study the relationship between strain and airway admittance. In Fig. 44 are plotted the strain as a function of frequency (a), the magnitude of wall admittance per unit length Yw as a function of frequency (b), the real part of Yw (c), and the imaginary part of Yw (d). The maximum in strain and magnitude of Yw occur at approximately the same frequencies, and the wall admittance shows an anti-resonance.
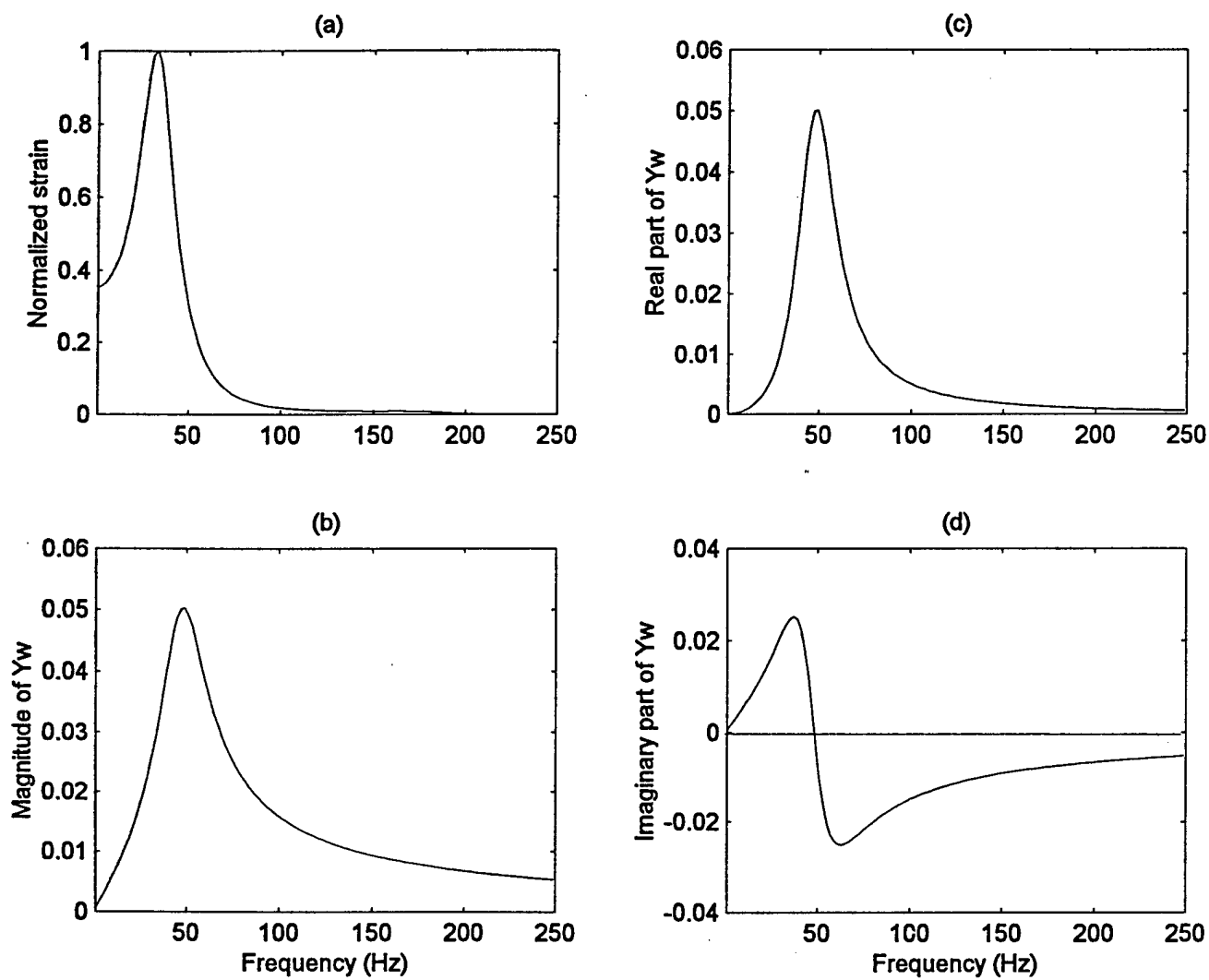
Figure 44. Relationship between strain and airway wall admittance (order 41 is taken as the representative.)

4.3 Simulations in asthmatic lung with comparison to those in normal lung

The Horsefield's asymmetrical model with upper airways was used to simulate Zin and Ztr in lungs with homogeneous peripheral airway obstruction and/or increase peripheral airway wall thickness (a model of asthma).

4.3.1 Comparison of Zin and Ztr of normal lung and with asthma

In the peripheral airways (i.e., d < 2 mm), we decreased diameters and/or increased wall thickness. Two different degrees of constriction were simulated, 40% and 60% decrease in airway diameters and two different increases in wall thickness were simulated, 40% and 60%. When the airways become constricted the frequency at which the acoustic anti-resonance occurred (at ~180 Hz) did not change, but the peak in the real and imaginary parts decreased as the level of bronchoconstriction increased (Fig. 45). The real part also became negatively frequency dependent at low frequencies with the highest level of bronchoconstriction.
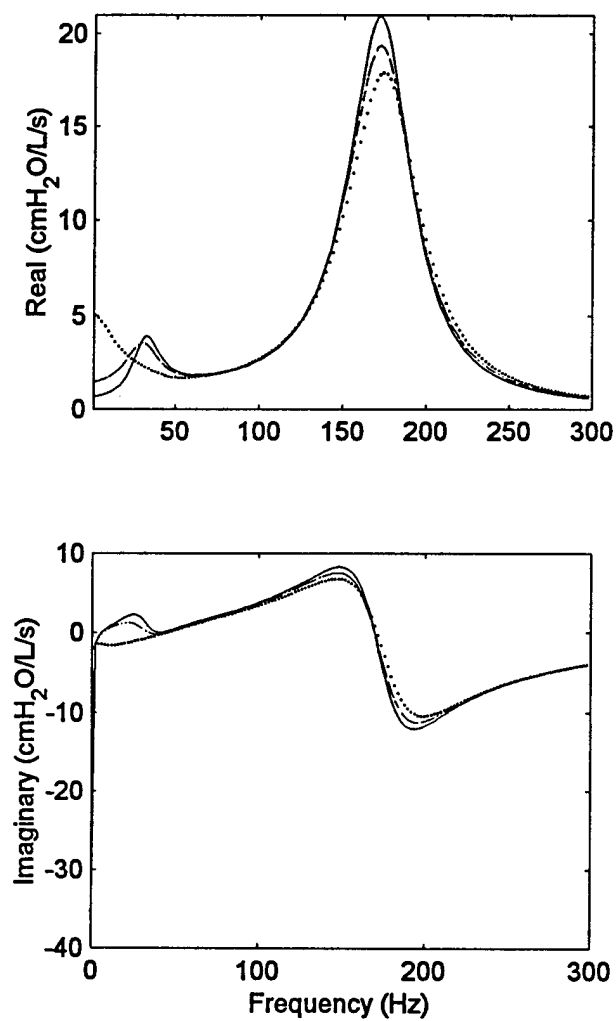
Figure 45. Comparison of Zin of normal lung (-), asthmatic lung with 40% constriction (--),

and asthmatic lung with 60% constriction (•).

We also simulated Ztr in healthy and asthmatic lung (Fig. 46) with 40% or 60% constriction, and/or 40% or 60% increase in airway wall thickness. The results of normal lung are compared in Fig. 46. From the magnitude of Ztr, airway constriction, compared to normal lung, increases the transfer impedance. When the airway wall thickness was increased by 40% or 60% in conjunction with airway constriction, there was little difference in Zin with constriction alone (Fig. 46).
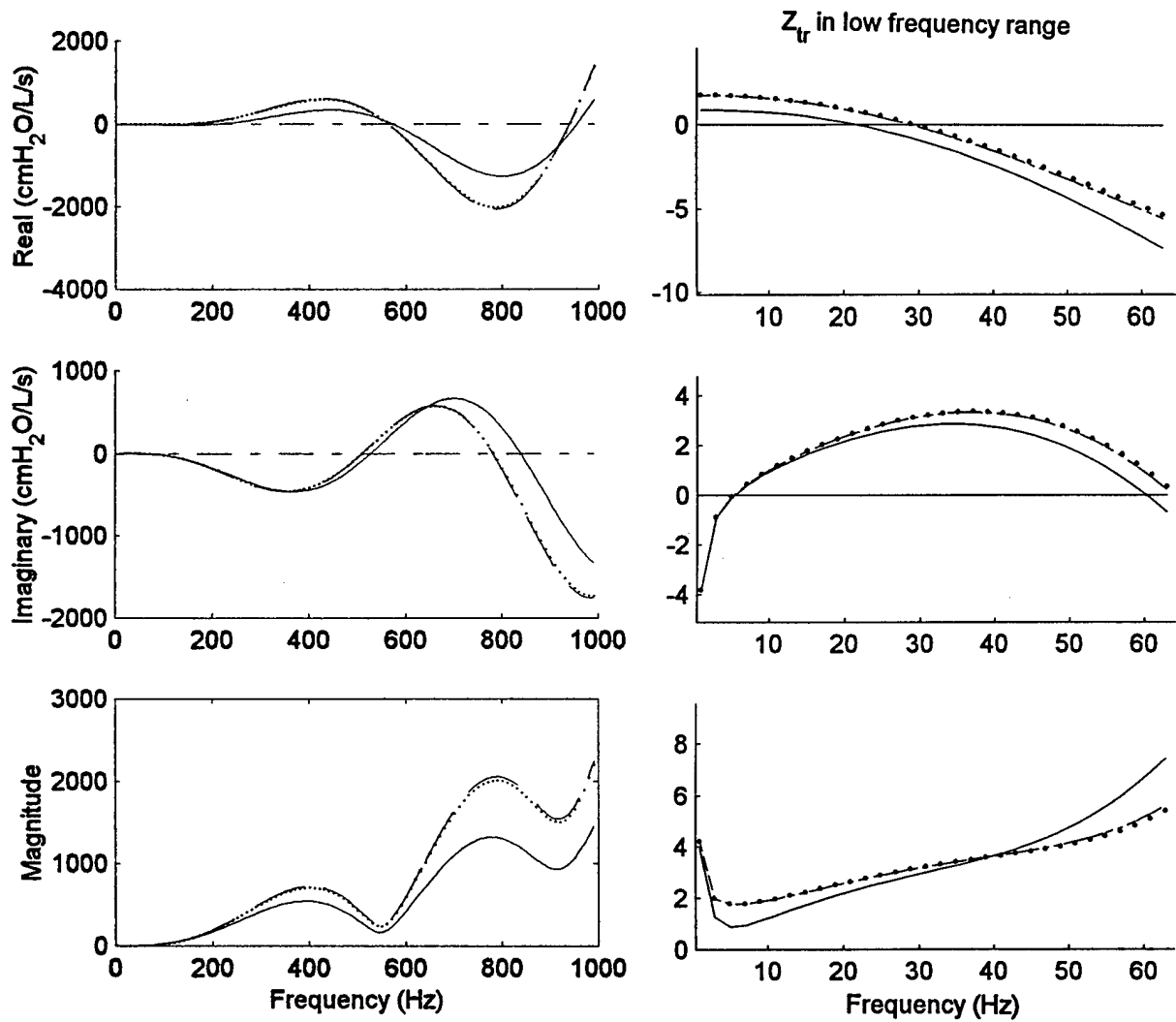
Figure 46. Comparison of Ztr of normal lung (-), asthmatic lung with 40% constriction

(--), and with 40% decrease in diameter alone (•).

4.3.2 Pressure ratio distribution with forced oscillation imposed at chest wall

We also predicted the pressure distribution within the lungs where the peripheral airways were constricted and/or their walls were thickened. The pressure ratio as a function of frequency and airway order was simulated along the shortest pathway (Fig. 47). Compared to the pressure ratios of the normal lung (Fig. 38), there is no significant change with constriction and/or increased wall thickness. The maximum pressure ratio is about 1.3, which is slightly smaller than the maximum pressure ratio in normal lung (about 1.6).
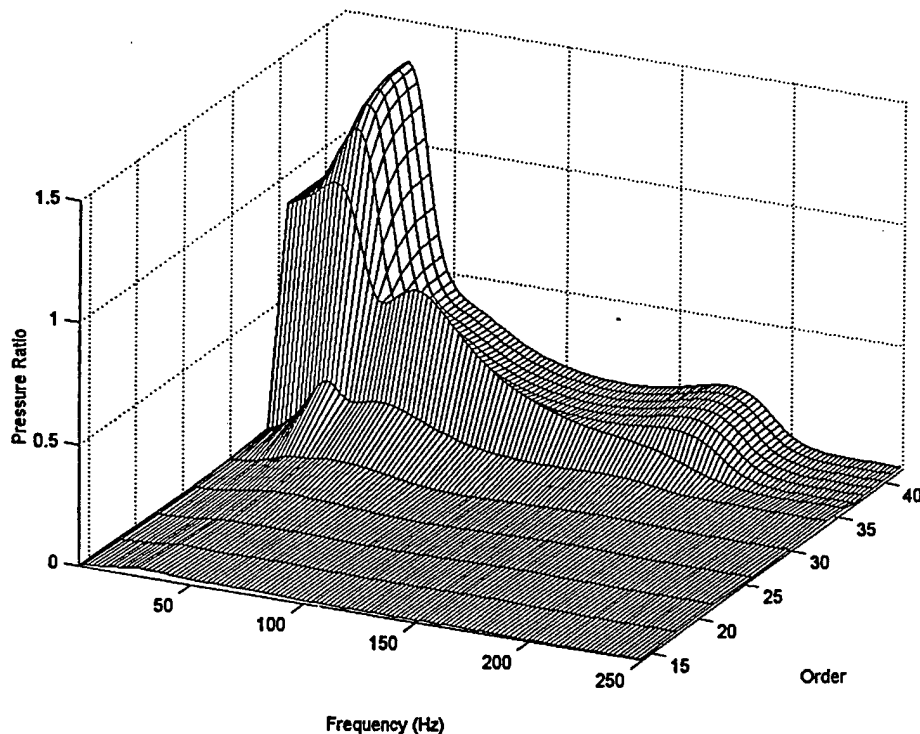
Figure 47. Pressure ratio distribution versus frequency and airway order along the shortest path in asthmatic lung

4.4 Simulation for Yeh's model of the rat lung

4.4.1 Zin and Ztr

We simulated Zin and Ztr for Yeh's model of the rat lung. Since Yeh's model is symmetrical, we used the analysis discussed in section 3.2. The lung volume was assumed to be13.7 ml [20]. The density, Young's modulus, and viscosity of the cartilage and soft tissue were assumed to be the same as those in the human model. Gas type was 100% humidified room air plus CO_2.

The results are shown in Fig. 48. The first resonant frequency was found to be approximately 90 Hz, and there were well-damped anti-resonances at approximately 5 kHz and 11 kHz. Both resonant and anti-resonant frequencies occurred at higher frequencies than in the human lung model. The reason is that the airway length of the rat lung is smaller than that of the human lung, which results in a shift of resonant and anti-resonant frequencies to higher frequencies. Similarly, the resonant and anti-resonant frequencies of Ztr shift to higher frequencies for the same reason (Fig. 49). The magnitude of transfer impedance increases almost monotonically with frequency.
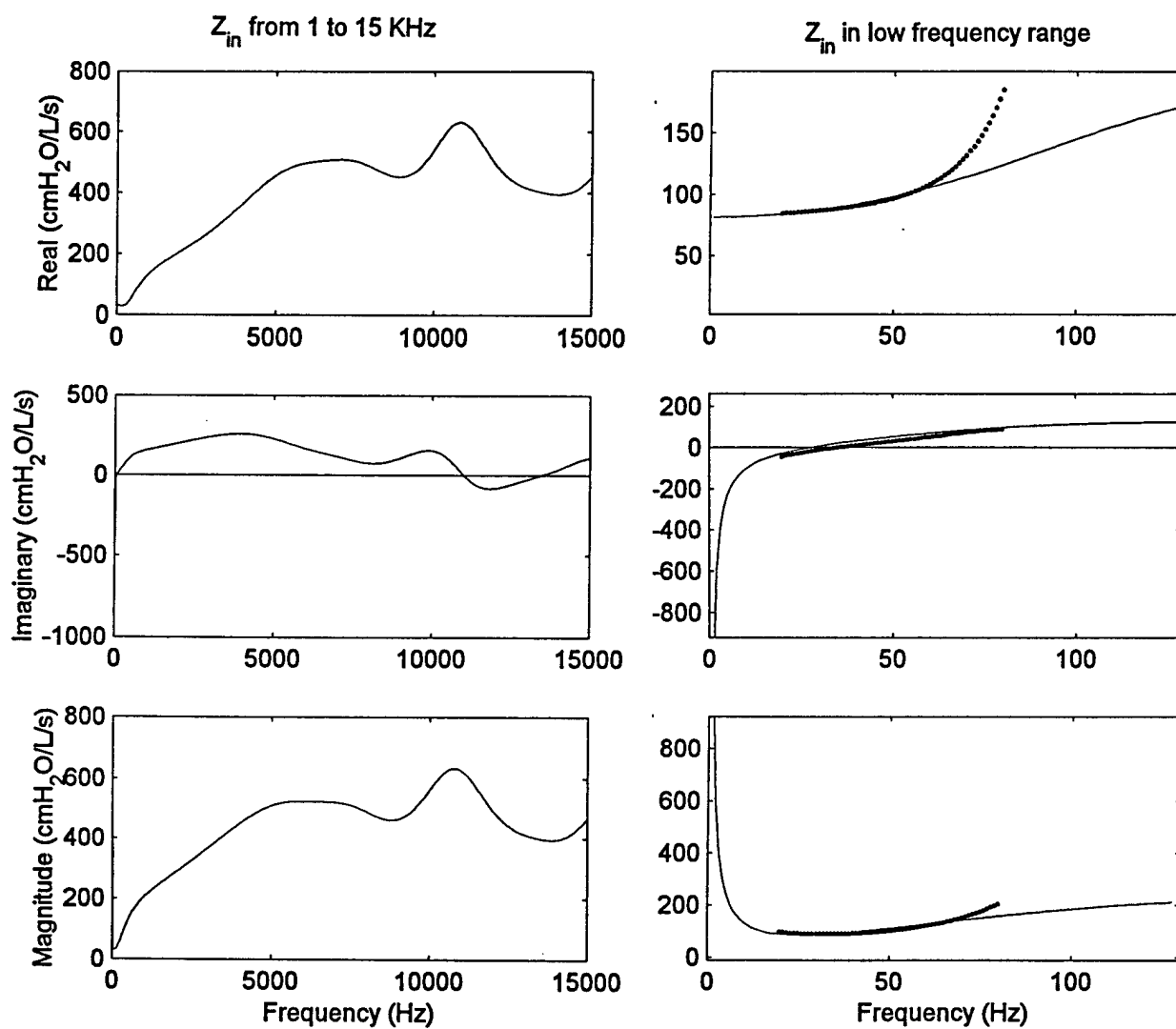
Figure 48. Zin of the Yeh's symmetrical model of the rat lung (-) and measured data

(•) (Jackson et al. [23])
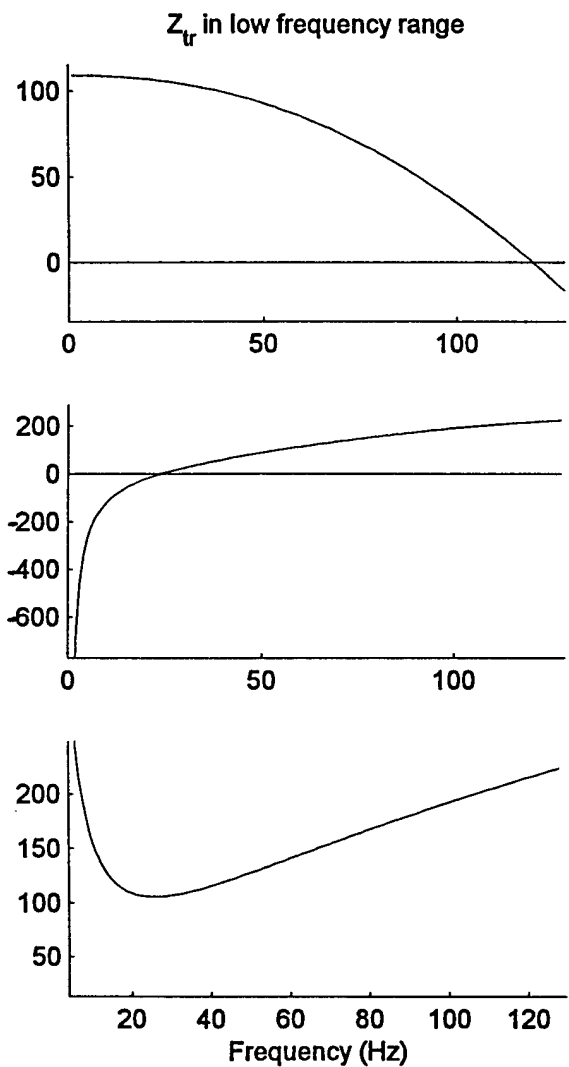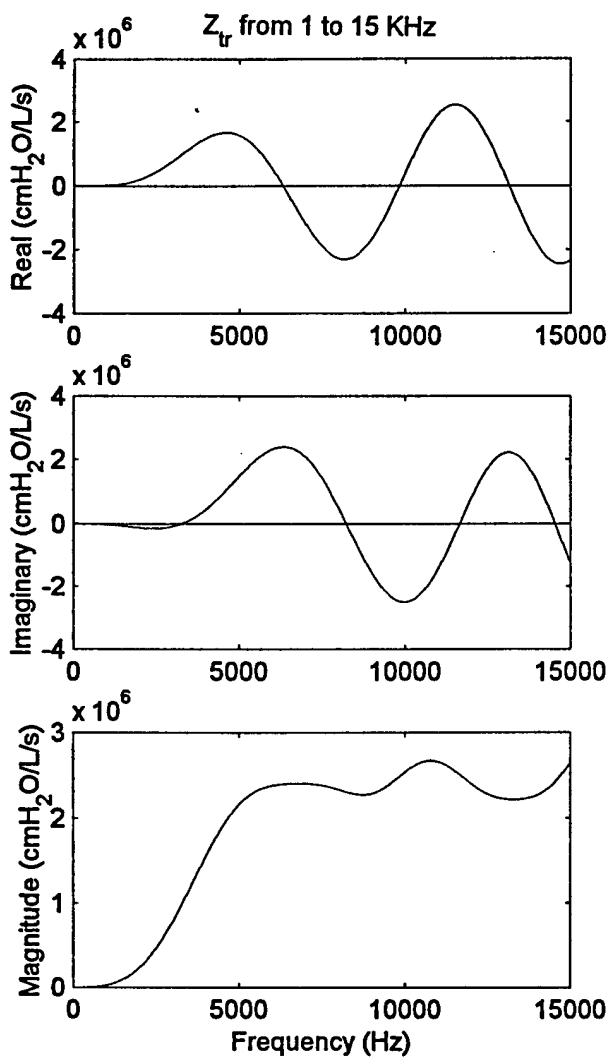
Figure 49. Ztr of the Yeh's symmetrical model of the rat lung

4.4.2 Pressure ratio with forced oscillation imposed at airway opening

The pressure ratio distribution with forced oscillation imposed at airway opening was simulated in a similar manner as was done for the human lung model. The result is shown in Fig. 50. As we can see from Fig. 50, the alveolar pressure is higher than that at the airway opening, which is similar to the findings in the human lung model. However, the frequency range over which pressure amplification occurs is larger ($1 < f < 100$ Hz) compared that in the human lung.
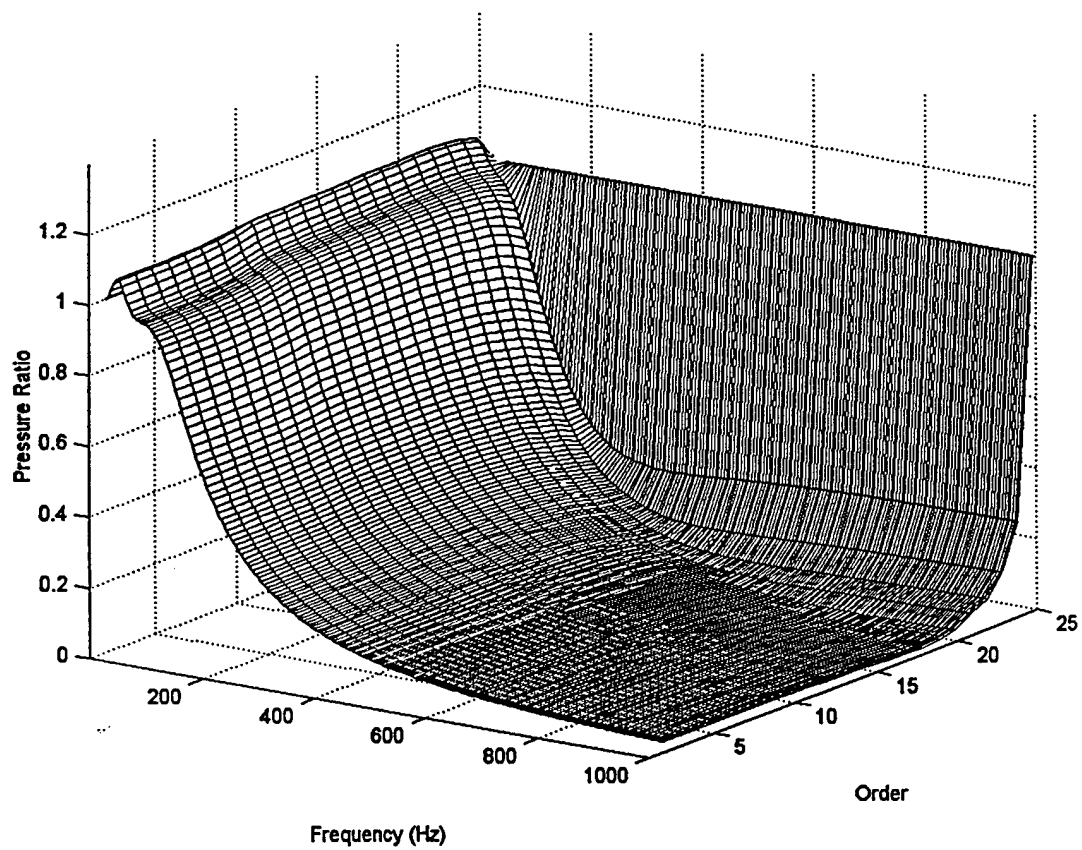
Figure 50. Pressure ratio distribution with forced oscillation imposed at the airway opening

4.4.3 Pressure ratio with forced oscillation imposed at chest wall

The pressure ratio distribution with forced oscillations imposed at the chest wall was also investigated in the rat lung model using the methods discussed in section 3.2 (Fig. 51). The pressure ratio is similar to that in the symmetrical human lung model. This might be due to the symmetry property of both airway networks.
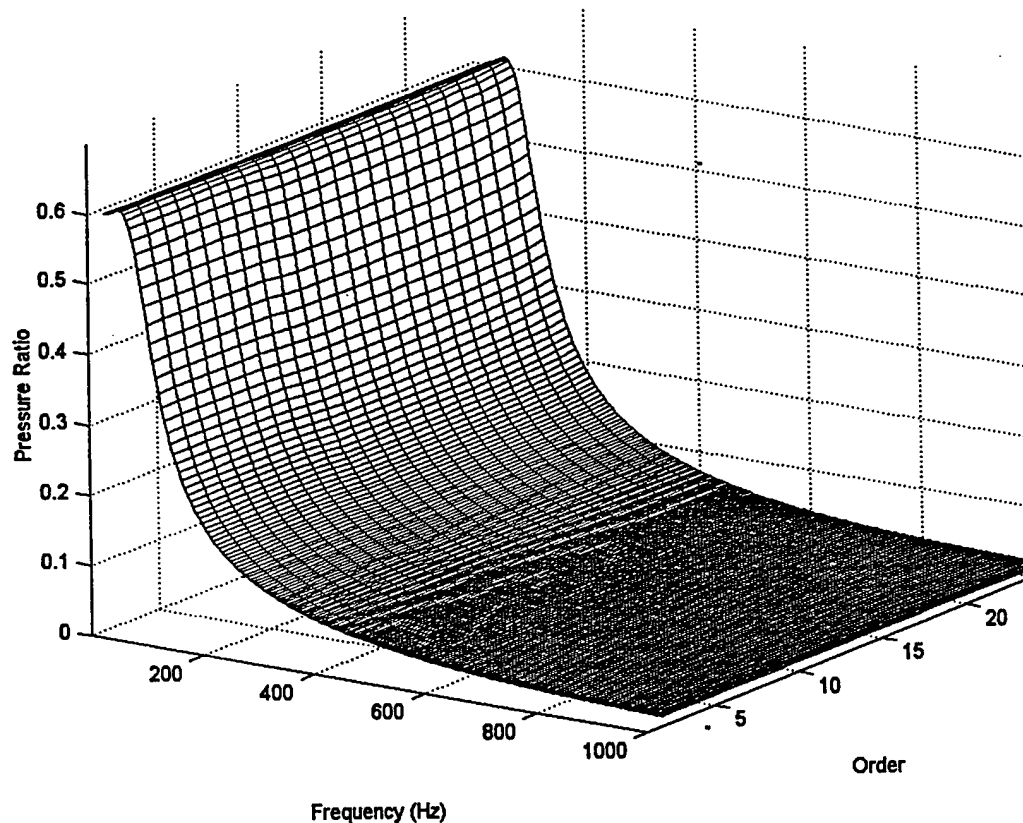
Figure 51. Pressure ratio distribution in the Yeh's rat lung model with forced oscillation imposed at chest wall.

94

5. Summary

We predicted input (Z_{in}) and transfer impedance (Z_{tr}), as well as pressure, strain, and wave propagation distribution using symmetrical and asymmetrical models of the human. The geometric structures, such as diameters and lengths of the airway, airway wall thickness, and branching patterns, are essential physical properties of the system and thus significantly influence impedance and pressure distributions. The two-port network model based on the symmetrical tree structure (i.e., the Weibel's model of the human lung and the Yeh's model of the rat lung) is relatively straightforward to realize. However, the resulting predictions may not be entirely appropriate since actual airways do not branch symmetrically. The prediction of pressure ratio, with forced oscillation imposed at the chest wall in the symmetrical airway network, did not indicate any pressure amplification. However, the predication using the superposition model based on the asymmetrically branched structure (i.e., the Horsefield's model of the human lung) showed that pressures in the central airways could be about 1.6 times that of the applied pressure.

The computational difficulty of the asymmetrical model was solved with the appropriately designed algorithms, the unique indexing representation of the airway structure, division of the airway network into symmetrical and asymmetrical zones, and further segmentation of the asymmetrical zone.

The Z_{in} and Z_{tr} predictions of the human lung models (both symmetrical and asymmetrical airway networks) compare closely to actual measurements in adult humans for frequencies between about 2-250 Hz, and 2-128 Hz, respectively. The predictions of pressure ratio, with forced oscillation imposed at the airway opening, of the symmetrical and asymmetrical airway network compare qualitatively to each other. With forced oscillation

imposed at the chest wall, pressure amplification (about 1.6 times that of the input pressure) was found at about 40 Hz in the central airways of the asymmetrical airway network of the human lung model. However, this was not found in the symmetrical human lung model. The first anti-resonant frequency was seen at about 90 Hz in the Z_{in} simulation of the rat lung model, and the first resonant frequency was seen at about 5 kHz. No pressure amplification was found in the rat lung model.

The reason for predicting the rat lung mechanics was to design experimental exposures to study the consequences of low frequency sound pressure applied to the body surface. However, our results indicate that the resonances and anti-resonances occur at extremely high frequencies compared to the human lung.

We also studied the consequences of airway constriction, i.e., as seen in asthmatic lungs. The amplitude of resistance at the anti-resonance decreases as the airways constrict more. However, in the low frequency region, the resistance increases with increasing constriction. The magnitude of transfer impedance also increases as airways constrict more.

Future work in this area of study can include applying the superposition model to the Horsefield's morphological data of the dog lung, since it has asymmetry and in common with the Horsefield's human lung model as well as the similar size.

The superposition model can be also modified to study the consequences of heterogeneous changes in airway, i.e., the constriction only occurs in left lobe of the lung with the right half normal.

Appendix A

1. Two network in parallel as an analogue to two airway branches having common upstream and downstream ends

When two airway branches are connected in parallel, a common pressure node exists at each junction, and the continuity must be satisfied at each junction. From Fig. 52, we can see that:

$$Q_u = Q_{u1} + Q_{u2} \tag{56}$$

$$Q_d = Q_{d1} + Q_{d2} \tag{57}$$

$$P_u = P_{u1} = P_{u2} \tag{58}$$

$$P_d = P_{d1} = P_{d2} \tag{59}$$
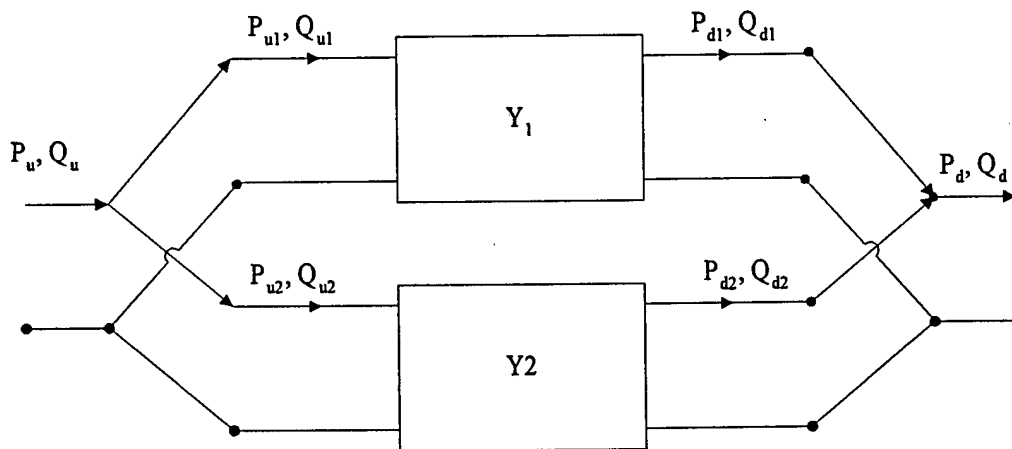
Figure 52. Two networks are connected in parallel

For network 1,

$$Q_1 = \begin{bmatrix} Q_{u1} \\ Q_{d1} \end{bmatrix} = [y_1] \begin{bmatrix} P_{u1} \\ P_{d1} \end{bmatrix} = [y_1] \cdot P_1 \qquad (60)$$

For network 2,

$$Q_2 = \begin{bmatrix} Q_{u2} \\ Q_{d2} \end{bmatrix} = [y_2] \begin{bmatrix} P_{u2} \\ P_{d2} \end{bmatrix} = [y_2] \cdot P_2 \qquad (61)$$

Compared to Eqns 60 and 61, we have

$$Q = Q_1 + Q_2 = ([y_1] + [y_2]) \cdot P = [y] \cdot P \qquad (62)$$

Namely,

$$[y] = [y_1] + [y_2] \qquad (63)$$

This can be extended to any number (say, *m*) of two ports connected in parallel as:

$$[y] = [y_1] + [y_2] + \cdots [y_m] \qquad (64)$$

2. Transformation from Y-matrix to T-matrix
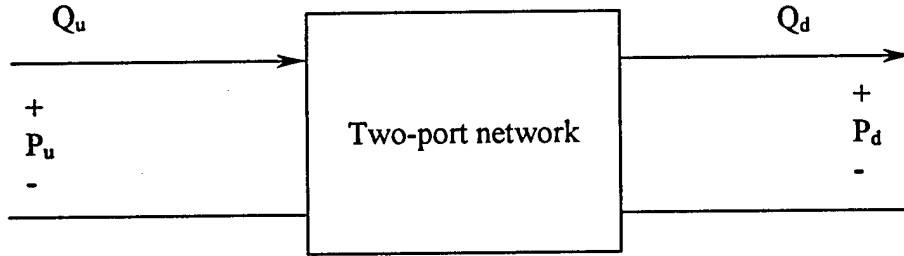
Figure 53. Two-port network. Note the signs of parameters depend on how the flows and pressures at two ends are defined.

The Y parameters for a network (Fig.53) are

$$
\begin{bmatrix} Q_u \\ Q_d \end{bmatrix} = \begin{bmatrix} y_{11} & y_{12} \\ y_{21} & y_{22} \end{bmatrix} \begin{bmatrix} P_u \\ P_d \end{bmatrix} \tag{65}
$$

Thus, we have

$$
Q_u = y_{11} \cdot P_u + y_{12} \cdot P_d \tag{66}
$$

$$
Q_d = y_{21} \cdot P_u + y_{22} \cdot P_d \tag{67}
$$

From Eq. 67, P_u can be expressed in terms of P_d and Q_d as

$$
P_u = -\frac{y_{22}}{y_{21}} \cdot P_d + \frac{1}{y_{21}} \cdot Q_d \tag{68}
$$

By substituting P_u in Eq. 66 and rearranging it, we have

$$P_u = -\frac{y_{11} \cdot y_{22} - y_{12} \cdot y_{21}}{y_{21}} \cdot P_d + \frac{y_{11}}{y_{21}} \cdot Q_d = -\frac{\Delta y}{y_{21}} \cdot P_d + \frac{y_{11}}{y_{21}} \cdot Q_d \qquad (69)$$

where Δy is the determinant of Y-matrix.

The T-parameters of the network are defined as

$$\begin{bmatrix} P_u \\ Q_u \end{bmatrix} = \begin{bmatrix} t_{11} & t_{12} \\ t_{21} & t_{22} \end{bmatrix} \begin{bmatrix} P_d \\ Q_d \end{bmatrix} \qquad (70)$$

Comparing Eqns. 68, 69 and 70, we have

$$T = \begin{bmatrix} t_{11} & t_{12} \\ t_{21} & t_{22} \end{bmatrix} = \begin{bmatrix} -\dfrac{y_{22}}{y_{21}} & \dfrac{1}{y_{21}} \\ -\dfrac{\Delta y}{y_{21}} & \dfrac{y_{11}}{y_{21}} \end{bmatrix} \qquad (71)$$

3. T-matrix of tissue properties

Consider the two-port network representation of tissue properties as shown in Fig. 54. Q_{cw} can be expressed in terms of P' and Q' as

$$Q_{cw} = \frac{P'}{Z_g} + Q' \qquad (72)$$

P_{cw} is obtained from Fig. 54

$$P_{cw} = P' + Z_{ti} \cdot Q_{cw} = P' + Z_{ti} \cdot \left(\frac{P'}{Z_g} + Q' \right)$$

$$= \left(1 + \frac{Z_{ti}}{Z_g} \right) \cdot P' + Z_{ti} \cdot Q_{cw} \tag{73}$$
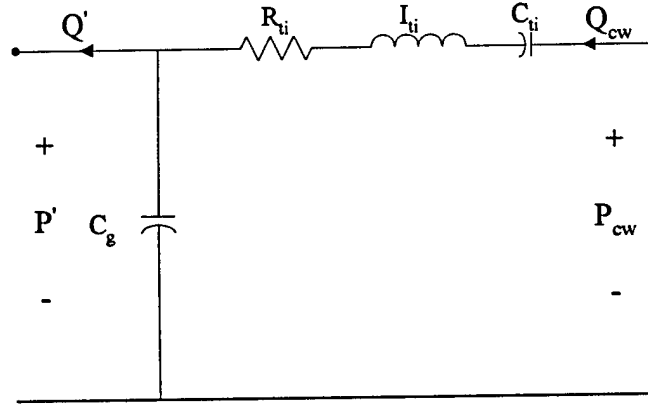

Figure 54. Two-port network representation of tissue properties

Thus, T-matrix for tissue properties is obtained from Eqns.72 and 73 as

$$\begin{bmatrix} P_{cw} \\ Q_{cw} \end{bmatrix} = T \cdot \begin{bmatrix} P' \\ P' \end{bmatrix} = \begin{bmatrix} 1 + \dfrac{Z_{ti}'}{Z_g} & Z_{ti} \\ \dfrac{1}{Z_g} & 1 \end{bmatrix} \cdot \begin{bmatrix} P' \\ P' \end{bmatrix} \tag{74}$$

4. Transformation between T-matrices

Consider Fig. 53 in Appendix A. 2. To compute P_d and Q_d for given P_u and Q_u, multiply Eq. 70 by the inverse of the T-matrix, T^{-1},

$$T^{-1} = \begin{bmatrix} t_{11} & t_{12} \\ t_{21} & t_{22} \end{bmatrix}^{-1} = \begin{bmatrix} t_{22} & -t_{12} \\ -t_{21} & t_{11} \end{bmatrix} \qquad (75)$$

Note that the determinant of the T-matrix is unity. We have

$$\begin{bmatrix} t_{11} & t_{12} \\ t_{21} & t_{22} \end{bmatrix}^{-1} \begin{bmatrix} P_u \\ Q_u \end{bmatrix} = \begin{bmatrix} t_{11} & t_{12} \\ t_{21} & t_{22} \end{bmatrix}^{-1} \begin{bmatrix} t_{11} & t_{12} \\ t_{21} & t_{22} \end{bmatrix} \begin{bmatrix} P_d \\ Q_d \end{bmatrix} \qquad (76)$$

Simplifying and reorganizing Eq. 76 gives us

$$\begin{bmatrix} P_d \\ Q_d \end{bmatrix} = \begin{bmatrix} t_{22} & -t_{12} \\ -t_{21} & t_{11} \end{bmatrix} \begin{bmatrix} P_u \\ Q_u \end{bmatrix} \qquad (77)$$

Therefore, P_d and Q_d can be computed as

$$P_d = t_{22} \cdot P_u - t_{12} \cdot Q_u \qquad (78)$$

$$Q_d = -t_{21} \cdot P_u + t_{11} \cdot Q_u \qquad (79)$$

REFERENCES:

1. Habib R. H., R. B. Chalker, B. Suki, and A. C. Jackson. "Airway geometry and wall mechanical properties estimated from subglottal input impedance in humans", *J. Appl. Physiol.* 77(1): 441-451, 1994.

2. William H. Hayt, Jr., Jack E. Kemmerly, *Engineering Circuit Analysis.* P76, 1986, McGraw-Hill Book Company.

3. Habib R. H., B. Suki, J. H.T. Bates, and A. C. Jackson. "Serial distribution of airway mechanical properties in dogs: effects of histamine", *J. Appl. Physiol.* 77(2): 554-566, 1994.

4. Jackson A. C., and K. R. Lutchen. "Physiological basis for resonant frequencies in respiratory system impedances in dogs", *J. Appl. Physiol.* 70: 1051-1058, 1991.

5. DuBois, A. B., A W. Brody, D. H. Lewis, and B. F. Burgess, Jr. "Oscillation mechanics of the lungs and chest in man." *J. Appl. Physiol.* 8: 587-594, 1956.

6. Lutchen, K. R. and B. Suki. "Understanding Pulmonary Mechanics Using the Forced Oscillations Technique. Emphasis on breathing frequency." *Bioengineering Approaches to Pulmonary Physiology and Medicine*, edited by Khoo. Plenum Press, New York, 1996: pp. 227-253.

7. Lutchen, K. R., J. R. Everett, A. C. Jackson. "Impact of frequency range and input impedance on airway-tissue separation implied from transfer impedance." *J. Appl. Physiol.* 74(3): 1089-1099, 1993.

8. Peslin, .R. and JJ Fredberg. "Oscillation Mechanics of the respiratory system." *Handbook of Physiology. The Respiratory System. Mechanics of Breathing.* Bethesda, MD: Am. Physiol. Soc., 1986, Section 3, Volume III, Part 1, Chapter 11, pp. 145-176.

9. Sullivan, A. "Low and high frequency transfer impedance measurements in humans." *Master's Thesis.* Boston University, Department of Biomedical Engineering, Boston, MA, 1995.

10. Helal M. A., K. C. Watts, and S.N. Sarwal. "Theoretical model for assessing haemodynamics in arterial networks which include bypass grafts." *Med. & Biol. Eng. & Comput.*, 1990, 28, pp.Yen. 465-473

11. Weibel, E. R. "Morphometrics of the lung." *Handbook of Physiology. Respiratory*, sect. 3, vol. I., edited by W. O. Fenn and H. Rahn. Washington, DC: Am. Physiol. Soc., 1964, pp. 299-305

12. Horsefield, K., and G. Cumming. "Angles of branching and diameters of branches in the human bronchial tree." *Bull. Math. Biophys.* 29: 245-259, 1967

13. Personal communication with Prof. Suki, BME department, Boston University

14. Nedwell, J. R., and S. J. Parvin. "The effects of low frequency sonar transmissions on divers and ichthyofauna: literature survey and initial experimental results." DRA(AWL) TM93721, Sept. 1993

15. Suki, B., R. H. Habib, and A. C. Jackson. "Wave propagation, input impedance, and wall mechanics of the calf trachea from 16 to 1600 Ha." *J. Appl. Physiol.* 75: 2755-2766, 1993

16. Peslin, R. and J. J. Fredberg. "Morphometry of airways" *The Respiratory System. Mechanics of Breathing.* Bethesda, MD: Am. Physiol. Soc., 1986, Section 3, Volume III, Part 1, Chapter 7, pp. 75-88.

17. Hayt, W. H. and J. E. Kemmerly. "Two-port networks." *Engineering Circuit Analysis,* McGraw-Hill Book Company, 1986, Chapter 16, pp. 458-485

18. Comroe, J. H.. "Physiological diagnosis." *Physiology of Respiration,* Year Book Medical Publishers, Inc., 1966, Chapter 21, pp 218

19. Lambert, R. K., A. R. Frey, A. B. Coppens, and J. V. Sanders. "A method for estimating the Young's modulus of complete tracheal cartilage rings." *J. Appl. Physiol.* 70: 1152-1159, 1991

20. Jackson, A. C., M. Tabrizi, M. I. Kotlikoff, and J. R. Voss. "Airway pressures in an asymmetrical branched airway model of the dog respiratory system." *J. Appl. Physiol.:* Respirat. Environ. Exercise Physiol. 57(4): 1222-1230, 1984

21. Guelke, R. W., and A. E. Bunn. "Transmission line theory applied to sound wave propagation in tubes with compliant walls." Acoustica 48: 101-106, 1981

22. Dorkin, H. L., K. R. Lutchen, and A. C. Jackson. "Human respiratory input impedance from 4 to 200 Hz: physiological and modeling considerations." *J. Appl. Physiol.* 64(2): 823-831, 1988

23. Jackson, A. C., and J. W. Watson. "Oscillatory mechanics of the respiratory system in normal rats." *Respiration Physiol.* 48: 309-322, 1982

24. Takezawa J., F. J., Miller, and J. O'Neil. "Single-breath diffusing capacity and lung volumes in small laboratory mammals." *J. Appl. Physiol.:* Respirat. Environ. Exercise Physiol. 48(6): 1052-1059, 1980

25. Zwart, A. and E. M. Hessel. "Oscillatory mechanics of the mouse respiratory system." Eur. Respir. Rev. 4: 19, 182-186, 1994

26. Habib, R. H. "Airway geometry and wall mechanical properties from respiratory acoustic impedance." *Ph.D.'s dissertation.* Boston University, Department of Biomedical Engineering, Boston, MA, 1989.